A modified spectral-velocity-based earthquake intensity measure for super high-rise buildings

Xiao Lai[1], Zheng He[1, 2, *], Yuanyuan Chen[1], Yantai Zhang[3], Zhenhui Li[1], Zhuang Guo[1], Ling Ma[4]
[1] Department of Civil Engineering, Dalian University of Technology, Dalian, China,
[2] State Key Laboratory of Coastal and Offshore Engineering, Dalian University of Technology, Dalian, China
[3] College of Civil Engineering, Nanjing Forestry University, Nanjing, China
[4] The Bartlett School of Sustainable Construction, University College London, London, U.K.
[*] Corresponding author: E-mail: hezheng@dlut.edu.cn; Tel and Fax: +86-411-84707500

Abstract:

To provide an efficient and stable connection between seismic hazards and structural demands of super high-rise buildings, a modified spectral-velocity-based intensity measure (IM) is proposed in a general manner with the combination coefficients and an optimal number of modes estimated through the non-uniform flexural-shear coupled model (FSM-MS). With numerous FSM-MSs generated from statistical ranges of vibration periods, the optimal number of modes is regressed for near-field and far-field ground motions, respectively. Utilizing seven structural models with different heights and dynamic properties, the performance of selected IMs is systematically studied in two stages. The superiority of the proposed IM in stable and high efficiency is obviously observed through seven FSM-MSs, together with the other 19 IMs. Its sufficiency and scaling robustness are fully demonstrated by two significantly distinct super high-rise buildings. The proposed IM is promising as a specialized and desirable tool in the seismic performance evaluation of super high-rise buildings.

Keywords: Earthquake intensity measure; super high-rise building; spectral velocity; flexural-shear coupled model; inter-story drift ratio.

1. Introduction

In the framework of performance-based earthquake engineering, ground motion intensity measures (IMs) have played an important role in establishing the link between motion-related parameters and response-based demand measures (DMs) of structures. Slender super high-rise buildings, compared with others, are likely to exhibit more complicated dynamic properties and complex earthquake responses as the result of dual mass-stiffness non-uniformities (Lai et al. 2021). It is hard to maintain a high-level efficiency of the link between the motion-related parameters and structural DMs by those IMs developed based on the background of structurally uniform low-rise and high-rise buildings. To reach a more credible seismic performance evaluation of those slender buildings, it is necessary to have an insight into the development of a more efficient, stable and generalized IM to cover a broader range of buildings.

The selection of an appropriate core element is the key part of constructing an IM. Compared with the amplitude and duration of ground motion, the spectral parameters that can be closely correlated with structural dynamic properties are more preferable. The spectral acceleration at the fundamental period $S_a(T_1)$, which indicates a link with equivalent lateral force, has become one of the most popular core elements since the 1990s (Shome and Cornell 1999). However, some $S_a(T_1)$-based IMs were observed not always to be effective for long-period structures or near-field ground motions, exhibiting a high variability in the DMs with a given IM (Luco and Cornell 2007; Eads et al. 2015). Some research activities turned to using other spectral parameters as the core elements in the IMs applied to super high-rise buildings. Based on the case study on two super high-rise buildings, Zhang et al. (2018) found that the correlation coefficients between the spectral velocities at the fundamental periods $S_v(T_1)$ and the maximum inter-story drift (ISD) ratios are much higher than those between the maximum ISD ratios and $S_a(T_1)$ and the spectral displacement at the fundamental period $S_d(T_1)$. Other studies (Ye et al. 2013; Lu et al. 2013; He and Lu 2019) observed a close relation between peak ground velocity (PGV) and the maximum ISD ratios of super high-rise buildings. As $S_v(T_1)$ approaches PGV if T_1 is extremely large (Chopra 2016), $S_v(T_1)$ is one promising core element in the IMs for the DM of the maximum ISD ratio.

The potential of using spectral velocity as a core element in the IMs has been recognized by some researchers. As one of the spectral velocity-based IMs, the Housner intensity (HI) (Housner 1952) is defined as the integral of the pseudo-velocity spectrum in the range from 0.1 to 2.5 s. Within the same integral interval, Thun (1988) replaced the pseudo-velocity spectrum with the spectral velocity in the proposed velocity spectrum intensity (VSI). The investigation by Yakut and Yılmaz (2008) indicated a close relation of VSI with the maximum ISD ratio. VSI was also able to effectively predict the maximum ISD ratio and top displacement of tall chimneys (Qiu et al. 2020). To correlate VSI with structural dynamic properties, Avşar and Özdemir (2013) put forward a modified VSI (MVSI) for seismically isolated bridges where the integral interval is defined as 0.5 to 1.25 times the isolation period. Obviously, MVSI is applicable for those fundamental mode-controlled structures. To account for the high-mode effect typically existing in both high-rise and super high-rise buildings, Zhang et al. (2018) proposed a spectral velocity-based combination-type IM S_v^* where the spectral velocities at the required lower vibration periods are included. The two case super high-rise buildings determine the number of required vibration modes and combination factors. The expression form and efficiency of S_{v}^{*} need to be identified further for more building cases.

The high-mode effect was also addressed in the IMs based on other spectral parameters, particularly spectral accelerations. In the proposed two multiple mode-based IMs, i.e., IM_{12} and IM_{123}, for the sake of simplicity, Vamvatsikos and Cornell (2005) assigned identical exponents to all the spectral accelerations involved. Based on the previously proposed $S_{\mathrm{a}}(T_1)$-based IM, I_{NP} (Bojórquez and Iervolino 2011), Bojórquez et al. (2017) further developed the IM of IB_{sa} in which the ratio R of high-mode spectral acceleration to $S_{\mathrm{a}}(T_1)$ was introduced and the constant exponent of R was calibrated by two 2D frames. In the multiple spectral displacement-based IM proposed by Luco and Cornell (2007), i.e., $IM_{1I\&2E}$, the dynamic combination coefficients were adopted. They are determined by the modal participation factors at the floor where the maximum ISD ratio takes place. In the development of the multiple spectral acceleration-based IM, i.e., S_{123}, by Su et al. (2017), the combination coefficients were determined as the modal mass participation factors in which the mode shapes and mass matrix of a structural finite element model are required. In addition to the combination coefficients, the determination of required (or optimal) vibration modes in these combination-type IMs is supposed to be case-independent as much as possible. Using the uniform flexural-shear coupled model (FSM-U) (Miranda and Taghavi 2005), Lu et al. (2013) established an approximate relation between the optimal vibration modes and the fundamental periods of six different structures in their proposed spectral acceleration-based IM of $\overline{S}_{\mathrm{a}}$. For computational efficiency, the combination coefficients of the spectral accelerations involved and the shear-flexural stiffness ratios α of the FSM-Us of all six structures were assigned with identical values. Zhang et al. (2018) further incorporated the merits of S_{123} and $\overline{S}_{\mathrm{a}}$ in their developed linear combination-type spectral acceleration-based IM of $\overline{S}_{\mathrm{a}}^{*}$ where the number of required vibration modes is determined by a couple of FSM-Us with different shear-flexural stiffness ratios α. However, the typical feature of mass-stiffness non-uniformities existing in super high-rise buildings was not well reflected in all the IMs mentioned above. In this case, the performance of these IMs might be subject to an apparent fluctuation. More importantly, the calibration of related parameters and verification was still not comprehensive.

To respond to this concern in a more efficient, stable and general way, for super high-rise buildings, a modified multiple spectral velocity-based IM called $\overline{S}_{\mathrm{v}}^{*}$ based on its precedent version (Zhang et al. 2018) was developed with the aid of the previously proposed non-uniform flexural-shear coupled model

(FSM-MS) (Lai et al. 2021). FSM-MS is employed to provide a quick estimate of the combination coefficients of $\bar{S}_{\mathrm{v}}^{*}$ and also to act as an analytically efficient tool in the determination of the optimal number of modes involved. The potential link between hysteretic energy dissipation and spectral velocity is discussed to make the modified IM more physics-based. Seven structural models with different heights covering a large range of vibration periods are included in developing the IM with FMS-MS. The performance and applicability of the are is observed systematically in two stages with deliberately selected sixty ground motions in the near-field and far-field groups. The preliminary investigation on the efficiency of the proposed modified IM, $\bar{S}_{\mathrm{v}}^{*}$, is carried out with seven FSM-MSs, together with other 19 IMs. The efficiency, sufficiency and scaling robustness of preliminarily qualified IMs are further observed by the inelastic time history analyses of two super high-rise buildings with significantly different heights and mass-stiffness non-uniformities.

2. Modified spectral-velocity-based intensity measure

2.1 Intensity measure with spectral velocity

Compared with spectral displacement and spectral acceleration, the spectral velocity is a better "seed" of combination-type IMs to correlate with the maximum ISD ratios of super high-rise buildings (Zhang et al. 2018), and the relationship between the spectral velocity and ground motion intensity can be illustrated in terms of the energy during vibration. For a single-degree-of-freedom system (SDOF), the kinetic energy E_{K}, viscous damping energy E_{C}, absorbed energy E_{A} and input energy of ground motion E_{I} at the end of the ground motion can be obtained by the integral of the relative motion differential equation with respect to the displacement response (Akiyama 1985). Housner (1956) defined the sum of E_{K} and E_{A} as the input energy attributable to damage E_{D}, and introduced the following equivalent velocity V_{D} of the E_{D}:

$$V_{\mathrm{D}} = \sqrt{\frac{2E_{\mathrm{D}}}{m_{\mathrm{SDOF}}}} = \sqrt{\frac{2\left(E_{\mathrm{K}}+E_{\mathrm{A}}\right)}{m_{\mathrm{SDOF}}}} \tag{1}$$

where, m_{SDOF} is the mass of the SDOF.

Housner (1956) believed that a conservative design scheme could be reached by assuming the spectral velocity to be the upper boundary of V_{D}. From the dynamic analysis of a nonlinear SDOF, Akiyama (1985) found that the spectral velocity is close to V_{D} rather than its upper boundary, indicating that E_{D} is approximately proportional to the square of the spectral velocity. That is, the spectral velocity is closely related to damage-related hysteretic energy dissipation. Fig. 1 further shows the correlation coefficients between the spectral velocities and spectral accelerations at the first four periods and the maximum ISD ratios of 61-story (S3) and 118-story (S5) super high-rise buildings under the two groups (i.e., near-field and far-field) of ground motions (see "Case study" section). Fig. 1 shows that the differences in the correlation coefficients mainly lie in the spectral velocity and spectral acceleration at the fundamental period of each building. Comparatively, the spectral velocities and spectral accelerations at the third and fourth periods are very close to each other for both S3 and S5. Although the spectral acceleration at the second period has a higher correlation coefficient than the spectral velocity at the second period in S5, it is reasonable to infer that the spectral velocity has a higher potential to be the core element of an IM with regard to super high-rise buildings. As indicated by Fig. 1, the spectral velocities at the higher-order periods are also well correlated with the maximum ISD ratios, especially for far-field ground motions. To reach a rational evaluation of the seismic performance of super high-rise buildings, the high-mode effect needs to be well addressed.

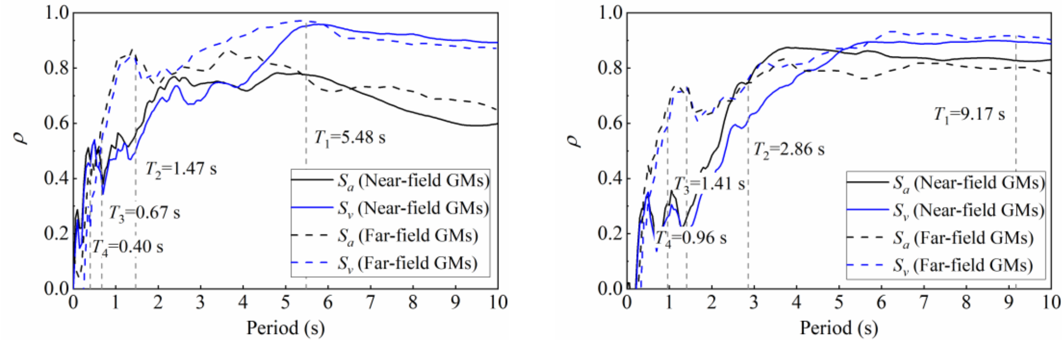

(a) S3 (b) S5

Fig. 1. Correlation coefficients between maximum ISD ratios and spectral velocities and spectral accelerations

The conceptual rationality of the combination of multimode spectral velocities can be physically addressed by modal pushover analysis (MPA). During MPA, due to the forced decoupling of modes, the E_D of a multi-degree-of-freedom system is equal to the sum of the $E_{D,n}$ of the equivalent SDOF of each mode with the assumption that mode shapes remain constant before and after the earthquake (Prasanth et al. 2008). Although the estimation accuracy of E_D depends on the degree of the nonlinear behavior of the structure, it is convincing that the E_D is still related to each $E_{D,n}$. Therefore, it is reasonable to formulate the IM based on the spectral velocities of multiple modes.

Due to the inherent randomness of ground motions and the unpredictability of structural nonlinear responses, it is impractical to theoretically construct an IM that can accurately predict the DM. In contrast, starting from the statistical law obtained from extensive studies in the past is more feasible to form an

IM conforming with engineering experience. Here, the following log-linear model about DM and IM (Shome and Cornell 1999) is adopted:

$$\ln(DM) = \ln a + b\ln(IM) + \ln(\varepsilon | IM) \tag{2}$$

where, a and b are the regressed coefficients; and $\varepsilon|IM$ is a random error.

For linear-elastic structures, as the input energy attributable to damage of each mode can be decoupled, the effect of the spectral velocity of each mode on the DM is independent of each other. Although this feature is not applicable to structures with strong nonlinear behaviors, for super high-rise buildings with sufficient safety margins and mild nonlinear behaviors under maximum considered earthquakes (MCE) (Lu et al. 2013), it can be assumed that the influences of spectral velocities on the DM are independent of each other in the IM. To reflect this in Eq. (2), the following combination-type IM with multiple spectral velocities is established by power functions:

$$\bar{S}_{\mathrm{v}}^{*} = \prod_{i=1}^{n} [S_{\mathrm{v}}(T_i)]^{\gamma_i} \tag{3}$$

where, γ_i is the combination coefficient of the i^{th} spectral velocity; and n is the number of modes.

According to Eq. (2), the γ_i in Eq. (3) can be regarded as the weighting factor of each spectral velocity to the DM, which is usually related to structural responses. In the modal decomposition method, response of the i^{th} mode depends on the corresponding equivalent lateral force, i.e., the product of the pseudo acceleration $A(T_i)$ and the inertia force distribution of the i^{th} mode $\mathbf{s}_i$ (Chopra 2016). The former describes the response over time and is reflected by the spectral velocity in Eq. (3). The ratio of the sum of all elements in the latter to the total structural mass is the modal mass participation coefficient, usually playing an important role in the determination of the number of modes in response history analysis (GB50011 2014). Moreover, it presents the proportion of the equivalent earthquake force corresponding to the i^{th} mode. In view of the above-mentioned physical background, and the consistency of the units between $\bar{S}_{\mathrm{v}}^{*}$ and the combination coefficients, the normalized modal mass participation coefficients are used as the combination coefficients γ_i (i=1, 2,…n), i.e.,

$$\gamma_i = \psi_i / \sum_{i=1}^{n} \psi_i \tag{4}$$

As mentioned above, the modal mass participation coefficients used in previous IMs (Su et al. 2017; Zhang et al. 2018) are determined based on the information of structural finite element models. Without such detailed information of structural finite element models, the modal mass participation coefficients cannot be obtained. However, with the common distribution of mass and stiffness along the height and the clear influence mechanism of macroscopic structural parameters on mode shapes, it is possible to obtain an analytical combination coefficient.

2.2 Analytical combination coefficient

The non-uniform flexural-shear coupled model (FSM-MS) in Fig. 2 simulates the flexural and shear deformation of the whole structure via a flexural beam and a shear beam, respectively, with the dual non-uniform distributions of mass and stiffness along the height (Lai et al. 2021). Compared with the previous flexural-shear coupled models with uniform properties (Miranda and Taghavi 2005) or only considering the non-uniform stiffness distribution (Alonso-Rodríguez and Miranda 2016), FSM-MS is more appropriate for super high-rise buildings. Since the analytical dynamic properties of FSM-MS exist, the combination coefficient can be expressed analytically.

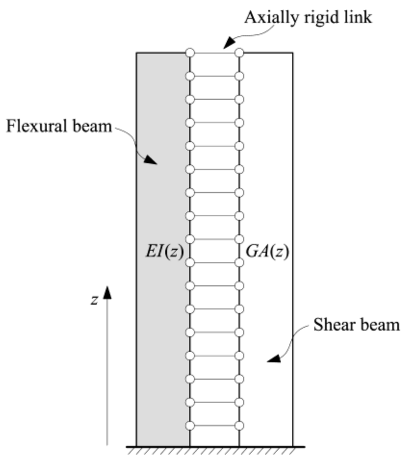

Fig. 2. Flexural-shear coupled model with non-uniform mass and stiffness

Based on the statistical data of some as-built super high-rise buildings, the linear density of FSM-MS is assumed to distribute linearly along the height, i.e., $\rho(x)=\rho_0[1\text{-}(1\text{-}\delta_\rho)x]$, and the flexural stiffness and shear stiffness can be approximately evaluated by $EI(x)=EI_0[1\text{-}(1\text{-}\delta_\rho)x]^3$ and $GA(x)=GA_0[1\text{-}(1\text{-}\delta_\rho)x]^2$, where x is the normalized height, i.e., x=0~1; δ_ρ is the non-uniform coefficient of the linear density, and ρ_0, EI_0 and GA_0 are the linear density, fleuxural stiffness and shear stiffness at the base, respectively (Lai et al. 2021). Based on these distribution functions and the balance of horizontal forces during free vibration, the following differential equation about the mode shape can be established:

$$\begin{aligned}&(1-cx)^2\frac{d^4\phi(x)}{dx^4}-6c(1-cx)\frac{d^3\phi(x)}{dx^3}+\left[6c^2+c\alpha^2x-\alpha^2\right]\frac{d^2\phi(x)}{dx^2}\\&+2\alpha^2c\frac{d\phi(x)}{dx}-\frac{\rho_0H^4}{EI_0}\omega^2\phi(x)=0\end{aligned} \tag{5}$$

where, H is the height of the structure; ω and $\phi(x)$ are the circular frequency and mode shape, respectively; c=1-δ_ρ; and α is the shear-flexural stiffness ratio defined as (Miranda and Taghavi 2005):

$$\alpha = H\sqrt{\frac{GA_0}{EI_0}} \tag{6}$$

The following modal shapes and vibration periods of FSM-MS can be analytically obtained by solving Eq. (5) via factorization (Lai et al. 2021):

$$T_i = 2\pi\sqrt{\frac{\rho_0 H^4}{\beta_i^2\left(\beta_i^2+\alpha^2\right)EI_0}} \tag{7}$$

$$\begin{aligned}\phi_i(x) = {} & D_{1,i}\frac{cJ_1\left[\frac{2\beta_i}{c}(1-cx)^{0.5}\right]}{2\beta_i(1-cx)^{0.5}} + D_{2,i}\frac{cY_1\left[\frac{2\beta_i}{c}(1-cx)^{0.5}\right]}{2\beta_i(1-cx)^{0.5}} \\ & + D_{3,i}\frac{cI_1\left[\frac{2\sqrt{\beta_i^2+\alpha^2}}{c}(1-cx)^{0.5}\right]}{2\sqrt{\beta_i^2+\alpha^2}(1-cx)^{0.5}} + D_{4,i}\frac{cK_1\left[\frac{2\sqrt{\beta_i^2+\alpha^2}}{c}(1-cx)^{0.5}\right]}{2\sqrt{\beta_i^2+\alpha^2}(1-cx)^{0.5}}\end{aligned} \tag{8}$$

where, $D_{1,i}$~$D_{4,i}$ are undetermined coefficients; and β_i is the dynamic characteristic coefficient corresponding to the i^{th} mode, which can be solved with the aid of the boundary condition.

Based on the mode shapes in Eq. (8) and the distribution function of the linear density, the i^{th} modal mass participation coefficient ψ_i in Eq. (4) can be rewritten as follows:

$$\psi_i = \frac{\left\{\int_0^1 \phi_i(x)\left[1-\left(1-\delta_\rho\right)x\right]dx\right\}^2}{\int_0^1 \phi_i^2(x)\left[1-\left(1-\delta_\rho\right)x\right]dx\int_0^1\left[1-\left(1-\delta_\rho\right)x\right]dx} \tag{9}$$

The dynamic properties of FSM-MS are controlled by the fundamental period T_1, α and δ_ρ, of a structure of concern, which can be efficiently calibrated by the procedure suggested by Lai et al. (2021). According to the procedure, δ_ρ is set as the ratio of the linear densities of the second story at the top and the first story at the base, and α is calibrated with the second-to-fundamental period ratio T_2/T_1 and δ_ρ as follows,

$$\alpha = \left[\frac{\left(T_2/T_1-\theta\right)\kappa^{1.954}}{\eta-\left(T_2/T_1-\theta\right)}\right]^{1/1.954} \tag{10}$$

where θ, η and κ are the regression coefficients related to δ_ρ, i.e., $\theta=(6.411+23.840\delta_\rho)^{-1/1.857}$, $\eta=\{0.148/[1-0.261\exp(-1.5\delta_\rho)]\}$ and $\kappa=\delta_\rho/(0.004+0.382\delta_\rho^{1.179})$.

The modes ϕ_i (i=1, 2, …, n) in Eq. (8) are associated only with α and δ_ρ (Lai et al. 2021). They become closely related to T_2/T_1 and δ_ρ by Eq. (10). As shown in Eqs. (4) and (9), the combination coefficients, γ_i (i=1, 2, …, n) are determined by ϕ_i (i=1, 2, …, n), δ_ρ and n. γ_i (i=1, 2, …, n) can be calculated once T_2/T_1, δ_ρ and n are known. As indicated by Eq. (3), in addition to ground motions, $\bar{S}_v^*$ depends on the first n vibration modes and corresponding combination coefficients γ_i (i=1, 2, …, n). The first n periods of FSM-MS can be evaluated by T_1, δ_ρ and α (or T_2/T_1) [see Eqs. (7) and (10)]. Thus, $\bar{S}_v^*$ corresponding to a ground motion of concern can be obtained by T_1, T_2/T_1, δ_ρ and n, without detailed information of structural models.

3. Optimal number of modes

3.1 Estimation procedure

To determine the optimal number of modes independent of specific structures, FSM-MS in Section 2.2 is adopted as the analysis model. With significant seismic fortification, the primary lateral force resisting components of well-designed super high-rise buildings usually remain elastic or exhibit slight yield under MCE instead of serious plastic behaviors (Lu et al. 2013). It is reasonable to believe that the optimal number of modes estimated by the elastic and inelastic analysis might be slightly biased. Since the elastic FSM-MS can rapidly estimate the maximum ISD ratio with high accuracy (Lai et al. 2021), it is acceptable to use FSM-MS to efficiently determine the optimal number of modes, which is estimated by the following Pearson correlation coefficient ρ between the natural logarithm of the maximum ISD ratio and $\bar{S}_v^*$:

$$\rho=\frac{m\sum_{j=1}^{m}x_j\cdot y_j-\sum_{j=1}^{m}x_j\cdot\sum_{j=1}^{m}y_j}{\sqrt{m\sum_{j=1}^{m}x_j^2-\left(\sum_{j=1}^{m}x_j\right)^2}\cdot\sqrt{m\sum_{j=1}^{m}y_j^2-\left(\sum_{j=1}^{m}y_j\right)^2}} \tag{11}$$

where, m is the number of selected ground motion records; y_j is the natural logarithm of the maximum ISD ratio under j^{th} record; x_j is the natural logarithm of the IM cooresponding to the j^{th} record; and ρ is usually distributed between -1 and 1, and the ρ approaching 1 denotes a better IM-DM positive correlation.

Based on the mode shape of FSM-MS in Eq. (8) and the modal decomposition method, the maximum ISD ratio, $IDR_{\max}$, is given by (Chopra 2016):

$$IDR_{\max}=\max_{x}\sum_{i=1}^{n}\Gamma_i D_i(t)\frac{d\phi_i(x)}{Hdx} \tag{12}$$

where, Γ_i is the modal participation coefficient corresponding to the i^{th} mode; and $D_i(t)$ is the displacement of the equivalent SDOF with T_i in Eq. (7).

Establishing FSM-MSs with reasonable parameters is the foundation of obtaining a credible optimal number of modes. As shown in Section 2.2, T_1, T_2/T_1 and δ_ρ are the dominant parameters of FSM-MS. δ_ρ cannot be set as 0 and 1 because of the numerical instability in solving dynamic properties (Lai et al. 2021), the architectural requirements for the floor area at the top story, and the self-weight reduction demand to ensure the ductility of vertical structural members. Since the δ_ρ of a 600-m super high-rise building is close to 0.26 (Lu et al. 2015), here the δ_ρ is taken from 0.2 to 0.9. T_1 is set from 1 s to10 s to include most buildings, even medium and high-rise buildings. The range of T_2/T_1 corresponding to each T_1 can be estimated by the following statistical relations among T_1, H, and the range of T_2/T_1 provided by Lai et al. (2021) based on 124 high-rise structures with heights from 100 to 650 meters:

$$T_1 = 0.1026H^{0.712} \tag{13}$$

$$\left(T_2/T_1\right)_{\mathrm{L}} = 0.123H^{0.120} \qquad \left(T_2/T_1\right)_{\mathrm{U}} = 0.179H^{0.120} \tag{14}$$

where, $(T_2/T_1)_{\mathrm{U}}$ and $(T_2/T_1)_{\mathrm{L}}$ are the upper and lower boundaries of T_2/T_1, respectively.

Utilizing Eqs. (13) and (14), Fig. 3 provides the procedure to estimate the optimal number of modes. Among the dominant parameters of FSM-MS, except T_2/T_1, T_1 and δ_ρ are chosen as the main variables in the procedure because of the higher contribution of the fundamental mode to the structural response and common application of T_1 to evaluate the structural lateral stiffness. To cover most T_2/T_1 corresponding to each T_1, T_2/T_1 takes 10 values with equal intervals in the range defined by Eq. (14). The optimal number of modes in each group of T_1 and δ_ρ is taken as the average of those obtained by different T_2/T_1 to consider each T_2/T_1 equally. The maximum number of modes $N_{\max}$ is taken as 8.

3.2. Ground motion selection

The optimal number of modes is estimated by the $IDR_{\max}$ under different ground motions. The criteria for selecting ground motions are as follows: 1) The primary vibration modes of super high-rise buildings may not be excited, because the low-frequency noise of the ground motions may be eliminated by accelerograph. To avoid this, the lowest frequency of the selected records should be lower than 0.1 Hz; 2) To induce as severe structural damage as possible, the evaluation of the IM's performance prefers strong ground motions, thus the smallest moment magnitude and PGA of the selected ground motion are set as 6 and 0.1 g; 3) Both far-field and near-field ground motions should be included for variability, and the source-to-site distance distinguishing between near-field and far-field ground motions is set as 20 km (Li and Xie 2007); 4) Featured with long-period velocity pulses mostly accredited to the forward directivity and fling step effect, the pulse-like near-field ground motions are more likely to result in devastating action on buildings with long fundamental periods (Kohrangi et al. 2019). Accordingly, in near-field ground motions, only those with velocity pulses are selected, which is accomplished by the wavelet-analysis-based method proposed by Baker (2007).

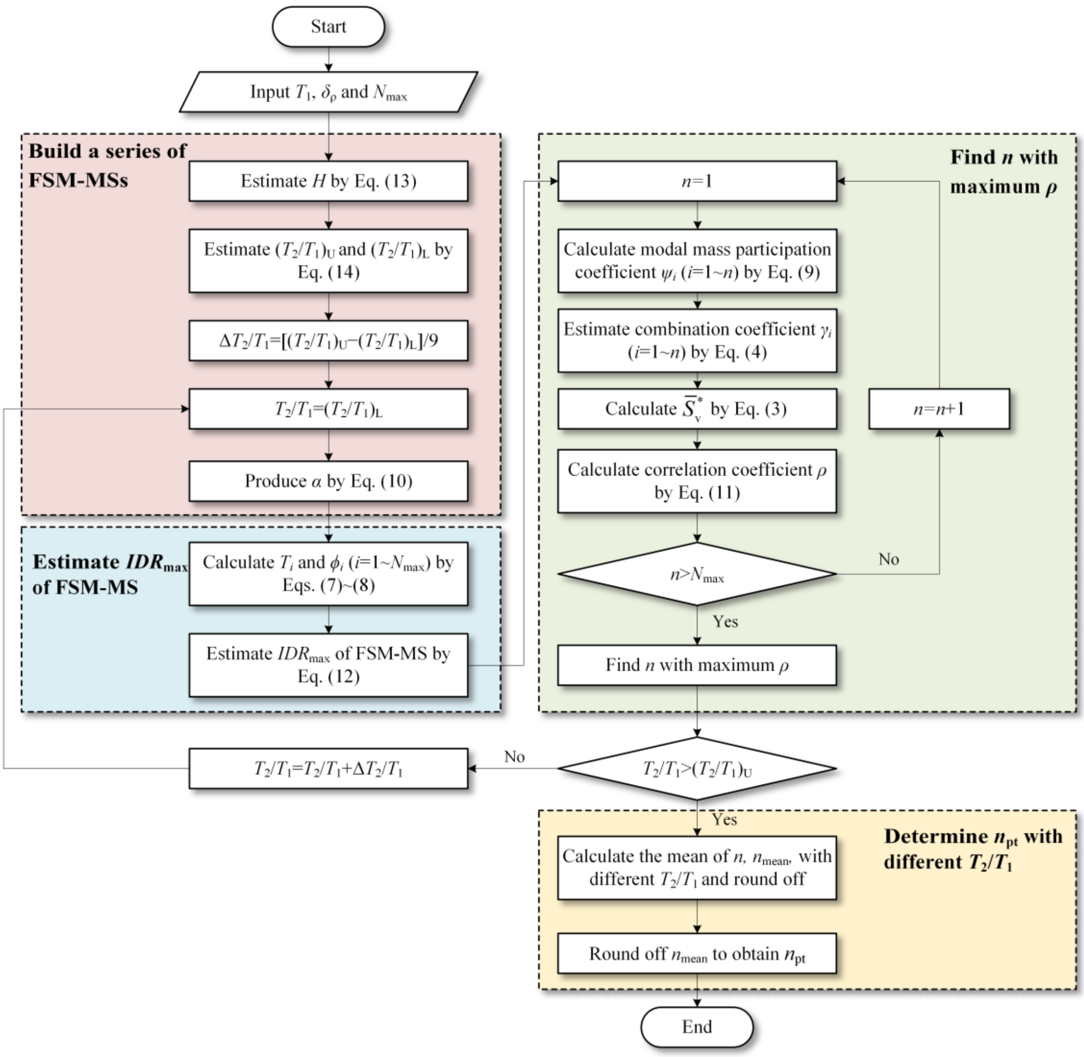

Fig. 3. Estimation procedure of optimal number of modes

Tables 1 and 2 list selected near-field and far-field ground motions from the NGA-West database of Pacific Earthquake Engineering Research (PEER) (Ancheta et al. 2014) with 30 motions for each. For far-field records, the PGA varies from 0.09 g to 0.69 g with an average of 0.28 g. For near-field records, the PGA varies from 0.13 g to 1.49 g with an average of 0.44 g. It can be seen that the selected ground motions are diverse in amplitude. To clearly obverse the contents of different frequency components in the selected records, Fig. 4 shows the corresponding Fourier amplitudes, where the horizontal coordinate is the logarithm of the frequency to the base 10, and the PGAs of the selected records are set to 0.035 g corresponding to the frequency-level earthquakes in areas with the 7-degree precautionary intensity (GB50011 2014). It can be seen that the frequencies of selected records are mainly between 0.1 Hz and

5Hz with various frequency components. Moreover, compared with far-field records, the Fourier amplitudes of near-field records between 0.1Hz and 0.4 Hz are significantly higher. Fig. 5 also provides elastic acceleration response spectra of selected records with a damping ratio of 5%. It is obvious that the near-field records produce a higher mean acceleration spectrum than far-field records. And the spectral accelerations of multiple near-field records exceed the mean spectrum in the long-period range due to the higher average PGA and more low-frequency components, which indicates that the selected near-field records may cause greater damage to super high-rise buildings.

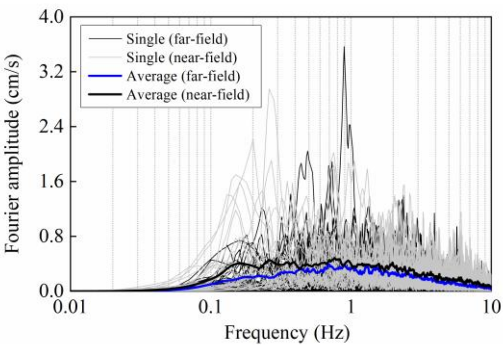

Fig. 4. Fourier amplitude of selected ground motions (PGA=0.035g)

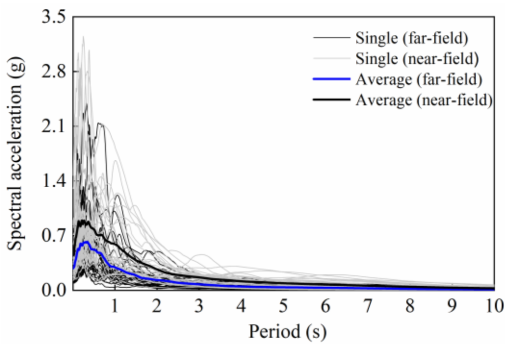

Fig. 5. Acceleration response spectra of selected ground motions (ξ=0.05)

3.3. Estimated results

Before providing the estimated optimal number of modes, the effect of the number of modes on the correlation coefficient ρ of $\overline{S}_{\mathrm{v}}^{*}$ should be figured out first. Here, FSM-MS corresponding to a 600-meter-high super high-rise building provided by Lai et al. (2021) is taken as an example to compare ρ with different numbers of modes as shown in Fig. 6. For FSM-MS, T_1=8.95 s, α=2.301, and δ_{p}=0.26. The damping ratio ξ is 0.05. It is apparent that ρ increases first and then decreases with the number of modes under both kinds of ground motions, and the optimal numbers of modes are both 3. As the correlation between $\overline{S}_{\mathrm{v}}^{*}$ and IDR_{max} depends on the modal mass participation coefficient ψ_i and the spectral velocity $S_{\mathrm{v}}(T_i)$ [see Eq. (3)], the values of ρ between the IDR_{max} and the $S_{\mathrm{v}}(T_i)$ of different modes are shown in Fig. 7 to explain this phenomenon. It can be seen that the significant reduction of the ρ between the higher-order $S_{\mathrm{v}}(T_i)$ and IDR_{max} occurs, which might be attributed to the weak increase and even reduction of IDR corresponding to the higher modes at the height where IDR_{max} is located. Because of the lower correlation of the higher-order $S_{\mathrm{v}}(T_i)$, the correlation of $\overline{S}_{\mathrm{v}}^{*}$ does not monotonically increase with the order of mode.

Table 1. Set of near-field ground motion records

No.	Earthquake	Year	Station	File name	M	R (km)	PGA (g)	PGV (cm/s)	PGD (m)	Lowest frequency (Hz)
1	Northridge-01	1994	Rinaldi Receiving Sta	RSN1063_NORTHR_RRS228	6.69	6.5	0.87	147.92	41.85	0.1
2	Northridge-01	1994	Sylmar - Olive View Med FF	RSN1086_NORTHR_SYL360	6.69	5.3	0.84	129.31	32.11	0.1
3	Kocaeli_ Turkey	1999	Arcelik	RSN1148_KOCAELI_ARE000	7.51	13.49	0.21	13.95	14.23	0.0875
4	Kocaeli_ Turkey	1999	Gebze	RSN1161_KOCAELI_GBZ270	7.51	10.92	0.14	32.63	29.75	0.1
5	Kocaeli_ Turkey	1999	Yarimca	RSN1176_KOCAELI_YPT060	7.51	4.83	0.23	69.68	62.29	0.0875
6	Chi-Chi_ Taiwan	1999	CHY024	RSN1193_CHICHI_CHY024-E	7.62	9.62	0.28	51.11	53.73	0.025
7	Chi-Chi_ Taiwan	1999	TCU060	RSN1499_CHICHI_TCU060-E	7.62	8.51	0.20	33.39	48.87	0.0375
8	Chi-Chi_ Taiwan	1999	TCU103	RSN1530_CHICHI_TCU103-E	7.62	6.08	0.13	70.22	68.35	0.0625
9	Chi-Chi_ Taiwan	1999	TCU122	RSN1546_CHICHI_TCU122-E	7.62	9.34	0.21	42.12	55.82	0.025
10	Duzce_ Turkey	1999	Bolu	RSN1602_DUZCE_BOL090	7.14	12.04	0.81	65.85	13.09	0.0625
11	Imperial Valley-06	1979	Brawley Airport	RSN161_IMPVALL.H_H-BRA225	6.53	10.42	0.16	36.59	25.66	0.05375
12	Imperial Valley-06	1979	EC County Center FF	RSN170_IMPVALL.H_H-ECC002	6.53	7.31	0.21	38.42	16.98	0.075
13	Imperial Valley-06	1979	El Centro Array #10	RSN173_IMPVALL.H_H-E10050	6.53	8.6	0.17	50.66	35.38	0.075
14	Imperial Valley-06	1979	El Centro Array #3	RSN178_IMPVALL.H_H-E03140	6.53	12.85	0.27	47.95	20.73	0.0625
15	Loma Prieta	1989	Los Gatos - Lexington Dam	RSN3548_LOMAP_LEX090	6.93	5.02	0.41	95.73	30.27	0.1
16	Bam_ Iran	2003	Bam	RSN4040_BAM_BAM-L	6.6	1.7	0.81	124.06	33.93	0.0625
17	L'Aquila_ Italy	2009	L'Aquila - V. Aterno -F. Aterno	RSN4482_L-AQUILA_CU104XTE	6.3	6.55	0.40	32.00	5.27	0.0625
18	L’Aquila Italy	2009	L’Aquila-Parking	RSN4483_L-AQUILA_AM043XTE	6.3	5.38	0.34	32.35	7.97	0.025
19	Chuetsu-oki_ Japan	2007	Joetsu Kakizakiku Kakizaki	RSN4847_CHUETSU_65010EW	6.8	11.94	0.46	89.00	28.22	0.0875
20	Darfield_ New Zealand	2010	DSLC	RSN6897_DARFIELD_DSLCN63E	7	8.46	0.24	67.22	81.24	0.075
21	Darfield_ New Zealand	2010	LINC	RSN6927_DARFIELD_LINCN23E	7	7.11	0.46	108.69	66.65	0.075
22	Darfield_ New Zealand	2010	Christchurch Resthaven	RSN6959_DARFIELD_REHSN02E	7	19.48	0.26	62.15	54.79	0.0625
23	Darfield_ New Zealand	2010	TPLC	RSN6975_DARFIELD_TPLCS63W	7	6.11	0.21	45.78	40.91	0.0625
24	Loma Prieta	1989	Gilroy Array #2	RSN766_LOMAP_G02000	6.93	11.07	0.37	34.74	9.50	0.075
25	San Fernando	1971	Pacoima Dam(upper left abut)	RSN77_SFERN_PUL164	6.61	1.81	1.22	114.41	39.00	0.0875
26	Christchurch_ New Zealand	2011	Christchurch Resthaven	RSN8123_CCHURCH_REHSS88E	6.2	5.13	0.72	86.53	26.97	0.1
27	El Mayor-Cucapah_ Mexico	2010	El Centro Array #12	RSN8161_SIERRA.MEX_E12360	7.2	11.26	0.33	72.57	54.62	0.05
28	Cape Mendocino	1992	Cape Mendocino	RSN825_CAPEMEND_CPM000	7.01	6.96	1.49	122.27	32.60	0.015
29	Cape Mendocino	1992	Petrolia	RSN828_CAPEMEND_PET000	7.01	8.18	0.59	49.30	16.59	0.07
30	El Mayor-Cucapah_ Mexico	2010	Westside Elementary School	RSN8606_SIERRA.MEX_CIWESHNN	7.2	11.44	0.26	55.20	46.849	0.05

Table 2. Set of far-field ground motion records

No.	Earthquake	Year	Station	File name	M	R (km)	PGA (g)	PGV (cm/s)	PGD (m)	Lowest frequency (Hz)
1	Kobe_ Japan	1995	Abeno	RSN1100_KOBE_ABN090	6.9	24.85	0.23	24.76	9.86	0.025
2	Kobe_ Japan	1995	Tadoka	RSN1118_KOBE_TDO000	6.9	31.69	0.30	24.48	7.58	0.0375
3	Gulf of Aqaba	1995	Eilat	RSN1144_AQABA_EIL-EW	7.2	44.1	0.09	13.78	6.52	0.0625
4	Kocaeli_ Turkey	1999	Atakoy	RSN1149_KOCAELI_ATK000	7.51	58.28	0.10	18.84	26.03	0.0375
5	Kocaeli_ Turkey	1999	Fatih	RSN1160_KOCAELI_FAT000	7.51	55.48	0.19	19.16	22.71	0.025
6	Kocaeli_ Turkey	1999	Zeytinburnu	RSN1177_KOCAELI_ZYT000	7.51	53.88	0.12	15.29	17.95	0.075
7	Chi-Chi_ Taiwan	1999	CHY008	RSN1183_CHICHI_CHY008-N	7.62	40.43	0.12	23.36	14.03	0.0375
8	Chi-Chi_ Taiwan	1999	CHY087	RSN1235_CHICHI_CHY087-E	7.62	28.91	0.14	10.23	7.67	0.0375
9	Chi-Chi_ Taiwan	1999	TCU045	RSN1485_CHICHI_TCU045-E	7.62	26.00	0.47	50.06	39.28	0.05
10	Chi-Chi_ Taiwan	1999	TCU095	RSN1524_CHICHI_TCU095-N	7.62	45.18	0.70	49.12	25.57	0.05
11	St Elias_ Alaska	1979	Icy Bay	RSN1628_STELIAS_059V2180	7.54	26.46	0.18	34.86	11.75	0.1
12	Imperial Valley-06	1979	Calipatria Fire Station	RSN163_IMPVALL.H_H-CAL225	6.53	24.6	0.13	15.59	13.25	0.0875
13	Imperial Valley-06	1979	Delta	RSN169_IMPVALL.H_H-DLT262	6.53	22.03	0.24	26.31	14.69	0.0875
14	Imperial Valley-06	1979	Niland Fire Station	RSN186_IMPVALL.H_H-NIL090	6.53	36.92	0.11	12.20	8.01	0.075
15	Coalinga-01	1983	Cantua Creek School	RSN322_COALINGA.H_H-CAK360	6.39	24.02	0.29	26.24	10.47	0.1
16	Borrego Mtn	1968	El Centro Array #9	RSN36_BORREGO_A-ELC180	6.63	45.66	0.13	26.69	14.57	0.1
17	Tottori_ Japan	2000	OKY005	RSN3908_TOTTORI_OKY005EW	6.61	28.82	0.34	19.78	6.42	0.0625
18	Tottori_ Japan	2000	SMN003	RSN3935_TOTTORI_SMN003NS	6.61	25.53	0.51	19.34	10.98	0.05
19	Niigata_Japan	2004	NIG023	RSN4213_NIIGATA_NIG023NS	6.63	25.82	0.40	24.81	6.98	0.075
20	Chuetsu-oki_Japan	2007	Joetsu Uragawaraku Kamabucchi	RSN4842_CHUETSU_65005EW	6.8	22.74	0.56	28.54	8.50	0.075
21	Chuetsu-oki_Japan	2007	Kashiwazaki City Takayanagicho	RSN4873_CHUETSU_65056EW	6.8	20.03	0.36	22.50	7.21	0.075
22	Chuetsu-oki_Japan	2007	Oguni Nagaoka	RSN4874_CHUETSU_65057EW	6.8	20.00	0.63	79.09	20.53	0.1
23	San Fernando	1971	LA-Hollywood Stor FF	RSN68_SFERN_PEL090	6.61	22.77	0.22	21.707	15.91	0.1
24	Superstition Hills-02	1987	Imperial Valley Wildlife Liquefaction Array	RSN729_SUPER.B_B-IVW090	6.54	23.85	0.18	31.65	22.26	0.1
25	Loma Prieta	1989	APEEL 2 - Redwood City	RSN732_LOMAP_A02043	6.93	43..23	0.27	53.63	13.31	0.075
26	Loma Prieta	1989	Hollister - South & Pine	RSN776_LOMAP_HSP000	6.93	27.93	0.37	62.97	32.29	0.0875
27	Loma Prieta	1989	Hollister Differential Array	RSN778_LOMAP_HDA165	6.93	24.82	0.27	44.22	19.69	0.0875
28	Loma Prieta	1989	Oakland-Outer Harbor Wharf	RSN783_LOMAP_OHW000	6.93	74.26	0.29	41.82	9.62	0.1
29	Landers	1992	North Palm Springs	RSN882_LANDERS_FHS000	7.28	26.84	0.14	11.15	4.63	0.05
30	Landers	1992	Yermo Fire Station	RSN900_LANDERS_YER270	7.28	23.62	0.24	51.10	41.69	0.07

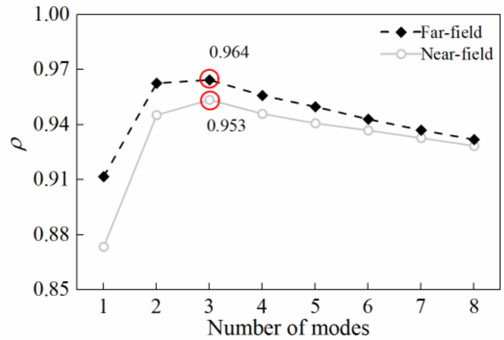

Fig. 6. Correlation coefficient of proposed IM with different numbers of modes (T_1=8.95s, α=2.301, δ_p=0.26, ξ=0.05)

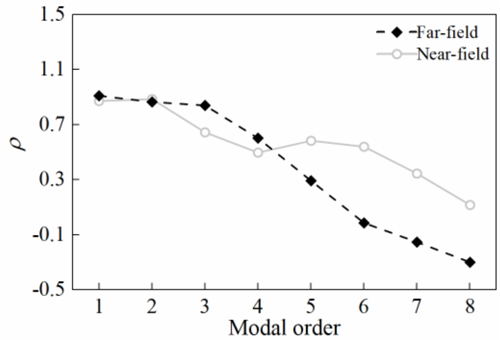

Fig. 7. Correlation coefficient of spectral velocity corresponding to different modes (T_1=8.95s, α=2.301, δ_p=0.26, ξ=0.05)

Following the procedure in Fig. 3, Fig. 8 shows the optimal number of modes n_{opt} with different T_1 and δ_p under near-field and far-field records. It can be seen that, for both kinds of records, with constant T_1, n_{opt} increases with smaller δ_p, which might be attributed to the increasing contribution of higher modes to structural responses. This phenomenon indicates that for structures with long fundamental periods, the influence of non-uniform distributions of mass and stiffness on the optimal modal number is non-negligible. In addition, n_{opt} rises with longer T_1 at a gradually decreasing speed. A possible explanation for this is that although the influence of higher modes is more significant to structures with long fundamental periods, the higher the mode, the weaker its influence compared with the accumulative influence of the lower modes. By comparing Fig. 8(a) and (b), it can be found that the optimal number of modes under near-field records is less than that under far-field records. According to the Fourier amplitude in Fig. 4, this difference can be explained by the higher contribution of the lower modes to the structural response under near-field records, where the proportion of low-frequency components is relatively higher. Another interesting finding is that when δ_p=0.9 and T_1=7~9 s, n_{opt}=1 under near-field records. In fact, based on Eq. (13), the height of the super high-rise buildings with T_1=7~9 s is about 370-540 m, and the corresponding δ_p is hardly greater than 0.9. This result is likely due to the following two reasons: 1) The number of existing super high-rise buildings with T_1>7 s is relatively small, and consequently the T_2/T_1 range in Eq. (14) may be greatly affected by the T_2/T_1 of structures with short and medium T_1. 2) Eq. (14) is obtained by logarithmic linear regression. The predicted value with the best accuracy is usually close to the mean of the variable, i.e., H. The closer to the boundary of the variable, the lower the prediction accuracy (Montgomery et al. 2012).

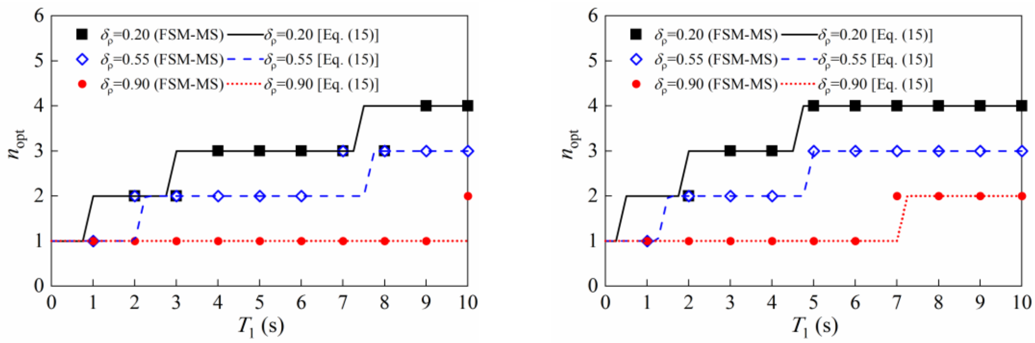

(a) Near-field ground motions (b) Far-field ground motions

Fig. 8. Optimal number of modes of proposed IM with different T_1 and δ_p

To quickly estimate n_{opt}, the relationship between n_{opt}, T_1 and δ_p under near-field and far-field records is fitted by the least-squares method. The maximum value of the regressed formula is set to 4 in light of the maximum n_{opt} according to Fig. 8. To reflect the gradually decreasing growth rate of n_{opt} with T_1, the following regressed formula is constructed by the exponential function:

$$n_{\mathrm{opt}} = \mathrm{INT}[4 - 3\delta_{\mathrm{p}}^{\varsigma T_1}] \tag{15}$$

where, INT means rounding off; ς is the coefficient obtained by the least-squares method, which is 0.151 and 0.242 for near-field and far-field ground motions, respectively; and the coefficients of determination R^2 in the regression are 0.878 and 0.916 for near-field and far-field ground motions, respetively.

Note that ς in Eq. (15) might be subject to some fluctuations for different ground motions. As the two groups of the ground motions (see Tables 1 and 2) deliberately selected have exhibited a high variability in both the amplitudes and frequency components, the obtained value of ς from these ground motions can be considered to be representative. Moreover, plenty of FSM-MSs used in the determination of the optimal number of modes cover a large range of building heights and dynamic properties. It could be believed that the dependency of Eq. (15) on FSM-MS with specific parameters is not obvious. With the combination coefficients in Eq. (4), the modal mass participation coefficient in Eq. (9) and the optimal number of modes in Eq. (15), the proposed IM $\overline{S}_v^*$ can be conveniently controlled by T_1, T_2/T_1 and δ_p. Compared with its previous version, i.e., $\overline{S}_a^*$ (Zhang et al. 2018), $\overline{S}_v^*$ can comprehensively address the effects of the mass-stiffness non-uniformities as well as the overall lateral stiffness and shear-flexure stiffness ratio. The adaptive combination coefficients and the optimal number of modes in $\overline{S}_v^*$ make it applicable for more general purposes. Thus, the versatility and stability of $\overline{S}_v^*$ in predicting the response-based DMs of buildings with various heights and structural systems is physically guaranteed.

4. Case study

It is computationally inefficient and practically infeasible to minimize the case dependency of the performance evaluation of the proposed IM via inelastic time history analyses (THAs) on a large number of elaborately-designed structural finite element models. To reach the same goal without the time-consuming inelastic THAs, the performance evaluation of the proposed IM is carried out in two stages. In the first stage, the selected 20 IMs (including the proposed IM) are preliminarily evaluated based on the ISD responses of seven elastic models predicted using FSM-MS. In the second stage, several IMs that passed the preliminary evaluation are comprehensively evaluated further by the inelastic THAs of two super high-rise buildings.

4.1 Basic information of model

Fig. 9 shows the basic information of the four super high-rise structures with different heights and non-uniformities of mass and stiffness. S1, S3, S5 and S7 have square, approximately oval, square and circular structural layouts, respectively. Comparatively, S5 and S7 exhibit obvious gradually tapered configurations along the height. The story heights of the standard floors of the four structures are 4.2 m, 4.2 m, 4.5 m and 4.5 m, respectively. Unlike S1, which adopts the pure frame-core tube structure, three, seven and eight strengthened stories with outriggers and belt trusses are placed in S3, S5 and S7, respectively. S5 even has mega bracings. Reinforced concrete beams (RCBs), columns (RCCs) and shear walls (RCSWs) are used in S1. S3 adopts circular concrete-filled steel tube columns (CCFSTCs) and steel-reinforced concrete shear walls (SRCSWs), which are connected with ordinary I-shaped steel beams (ISBs) or outriggers assembled by square steel tubes (SSTs). In S5 and S7, SRCSWs, steel-reinforced concrete columns (SRCCs) and H-shaped steel bracings (HSBs) are the main structural components. According to the Chinese seismic design code (GB50011 2014), the design peak ground accelerations (PGAs) of S1, S3, S5 and S7 are 0.98 m/s^2, 1.96 m/s^2, 0.98 m/s^2 and 0.98 m/s^2. And the characteristic periods of sites are 0.35 s, 0.55 s, 0.35 s and 0.90 s, respectively. Except for S_1 with a damping ratio of 0.05, the damping ratios of the others are 0.04. All the beams and columns of the four finite element models are simulated by the displacement-based fiber beam-column element (Spacone 1996), where the behaviours of the steel and concrete are simulated by the isotropic strain hardening model (Filippou et al. 1983) and the linear tension softening model (Mohd-Hisham 1994), respectively. The shear walls and floors are simulated by an improved multi-layered shell element considering large deformations (He and Sun 2018). To reduce the number of degrees of freedom, all the floors are assumed to be in-plane rigid, and the story-height multi-layered shell elements are used. The values of T_1 of S1, S3, S5 and S7 are 3.48

s, 5.48 s, 9.17 s and 8.95 s, while the values of T_2/T_1 are 0.221, 0.269, 0.312 and 0.318, respectively. The values of δ_ρ of S1, S3, S5 and S7 are 0.75, 0.77, 0.53 and 0.26, respectively. More detailed design information can be found elsewhere (Fu et al. 2015; Lu et al. 2015; Lai et al. 2021).

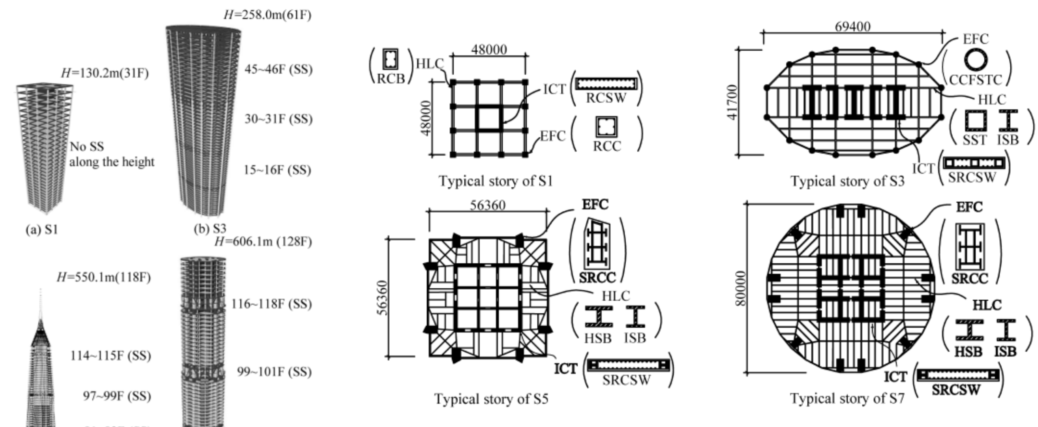

Table. Material and main size of structural components

	EFC		ICT		HLC	
	Materal	Main Size (mm)	Materal	Main Size (mm)	Materal	Main Size (mm)
S1	C40~C30	1250~620	C30	900~500	C30	600
S3	C60	1600~800	C60	800~400	Q345	400 (SST) 1000~800 (ISB)
S5	C60	6500~2000	C60	1500~500	Q345	1700~900 (HSB) 1000~600 (ISB)
S7	C70~C50	5300~2400	C60	1200~500	Q345	1700~900 (HSB) 1000~600 (ISB)

Fig. 9. Basic information of S1, S3, S5 and S7

To increase the diversity of the newly added FSM-MSs, the three new FSM-MSs, namely S2, S4, and S6, are established according to the average T_1, T_2/T_1 and δ_ρ of S1 and S3, S3 and S5, and S5 and S7, respectively. Without corresponding finite element models, the heights and total mass of the added FSM-MSs are set as the mean value of their parent structures. Table 3 presents the parameters of the FSM-MSs of S1~S7. It can be seen that, from S1 to S7, the values of T_1 and δ_ρ gradually increase in general. The α of FSM-MSs are calibrated by T_2/T_1, δ_ρ and Eq. (10). With the linear distribution function, the linear density at the base ρ_0 can be estimated by the total mass. After calculating the dynamic characteristic parameter β_1 by boundary conditions, EI_0 are determined by Eq. (7), and the corresponding GA_0 is obtained by Eq. (6).

Table 3. Parameters of FSM-MSs corresponding to S1~S7

Parameters	S1	S2	S3	S4	S5	S6	S7
Total weight ($\times 10^5$kN)	2.81	10.70	18.59	47.75	77.00	73.85	70.70
ρ_0 ($\times 10^5$kg/m)	2.53	6.39	8.65	14.62	15.60	18.62	18.40
$\rho(x)$ ($\times 10^5$kg/m)	1.89~2.53	4.25~5.59	6.66~8.65	9.50~14.62	8.21~15.60	7.45~18.62	4.79~18.40
δ_ρ	0.75	0.76	0.77	0.65	0.53	0.40	0.26
H (m)	130.20	194.10	258.00	404.05	550.10	578.10	606.10
EI_0 ($\times 10^{10}$kN·m^2)	1.01	4.98	10.26	49.12	102.29	199.81	334.68

GA_0 ($\times 10^6$kN)	1.49	7.65	14.77	37.32	49.29	57.83	48.24
α	1.58	2.41	3.10	3.52	3.82	3.11	2.30

Table 4 provides the first five periods and modal mass participation coefficients of the finite element models and corresponding FSM-MSs. Except for T_4 and T_5 of S5 and S7, the estimated vibration periods of FSM-MSs remain high accuracy. This discrepancy might be attributed to the more severe sensitivity of higher modes to the equipment of strengthened stories and more outriggers. The influence of the relative errors of T_4 and T_5 on $\overline{S}_{\mathrm{v}}^{*}$ should be slight because of the lower γ_i of higher modes. For the modal mass participation coefficient, except for the ψ_2 of S5 and S7, the errors of other ψ_i are not obvious in other cases. Based on the definition of ψ_i in Eq. (9), the accumulative deviation of the mode shape along the height might be the reason for the discrepancy. As a highly abstract simplified analytical model, the accuracy of the vibration periods and modal mass participation coefficients estimated by FSM-MS is acceptable.

Table 4. The first five periods and modal mass participation coefficients of finite element models and corresponding FSM-MSs

Model		T_1(s)	γ_1	T_2(s)	γ_2	T_3(s)	γ_3	T_4(s)	γ_4	T_5(s)	γ_5
S1	FEM	3.48	0.61	0.77	0.19	0.32	0.08	0.18	0.04	0.12	0.02
	FSM-MS	3.48	0.59	0.77	0.17	0.30	0.07	0.16	0.04	0.10	0.02
S2	FSM-MS	5.48	0.63	1.47	0.15	0.63	0.07	0.34	0.04	0.21	0.02
S3	FEM	5.48	0.63	1.47	0.17	0.67	0.07	0.40	0.04	0.24	0.02
	FSM-MS	5.48	0.63	1.47	0.15	0.63	0.07	0.34	0.04	0.21	0.02
S4	FSM-MS	7.33	0.61	2.13	0.15	0.95	0.07	0.52	0.34	0.33	0.02
S5	FEM	9.17	0.56	2.86	0.24	1.41	0.07	0.96	0.04	0.65	0.03
	FSM-MS	9.17	0.59	2.86	0.15	1.32	0.07	0.74	0.04	0.47	0.03
S6	FSM-MS	9.07	0.54	2.85	0.16	1.30	0.08	0.72	0.05	0.45	0.03
S7	FEM	8.95	0.49	2.85	0.27	1.42	0.10	0.91	0.04	0.65	0.02
	FSM-MS	8.95	0.47	2.85	0.18	1.29	0.09	0.71	0.05	0.45	0.03

4.2. Preliminary comparison of multiple intensity measures

Efficiency, sufficiency and scaling robustness are common criteria for evaluating the performance of IMs. The preliminary comparison focuses on the efficiency, because with enough sufficiency and scaling robustness, the more effective IM is preferred to predict the DM with high accuracy, which is crucial to the ground motion selection and reduction of the number of records required to obtain a reliable estimate of seismic responses. The IMs with high efficiency but inadequate sufficiency and scaling robustness can be identified through further comparison based on detailed finite element models.

To make a comparison with the proposed IM, some IMs are also selected in this study as shown in Table 5. In addtion to PGA, PGV and $S_{\mathrm{a}}(T_1)$, which are widely applied in some national design codes due to their convenience and simplicity, twelve IMs based on multiple spectral accelerations and four IMs

Table 5. Ground motion intensity measures in preliminary comparison

Reference	Intensity measure	Note
GB50011 (2014)	PGA	
JBSL (2005)	PGV	
Shome and Cornell (1999)	$S_a(T_1)$	
Cordova et al. (2001)	$S^* = [S_a(T_1)]^{1/2}[S_a(2T_1)]^{1/2}$	
Lu et al. (2013)	$\bar{S}_a = [\prod_{i=1}^{n} S_a(T_i)]^{1/n}$	The number of modes n is linearly dependent on T_1, and it is 3 for S1~S3, 4 for S4, and 5 for S5~S7.
Zhang et al. (2018)	$\bar{S}_a^* = \sum_{i=1}^{n} \psi_i S_a(T_i)$	With the suggested piecewise linear relation between n and T_1, n is 3 for S1~S7. ψ_i is the i^{th} modal mass participation coefficient.
Su et al. (2017)	$S_{12} = [S_a(T_1)]^{\psi_1/(\psi_1+\psi_2)}[S_a(T_2)]^{\psi_2/(\psi_1+\psi_2)}$	ψ_i is the i^{th} modal mass participation coefficient.
	$S_{123} = [S_a(T_1)]^{\psi_1/(\psi_1+\psi_2+\psi_3)}[S_a(T_2)]^{\psi_2/(\psi_1+\psi_2+\psi_3)}[S_a(T_3)]^{\psi_3/(\psi_1+\psi_2+\psi_3)}$	ψ_i is the i^{th} modal mass participation coefficient.
Lin et al. (2010)	$S_{N1} = [S_a(T_1)]^{1/2}[S_a(1.5T_1)]^{1/2}$	
	$S_{N2} = [S_a(T_1)]^{3/4}[S_a(T_2)]^{1/4}$	
Vamvatsikos and Cornell (2005)	$M_{12} = [S_a(\tau_{g1},5\%)]^{1/2}[S_a(\tau_{g2},5\%)]^{1/2}$	For high-rise structures, $\tau_{g1}= T_1$ and $\tau_{g2}= T_2$
	$IM_{123} = [S_a(T_1,5\%)]^{1/3}[S_a(T_2,5\%)]^{1/3}[S_a(T_3,5\%)]^{1/3}$	
Kazantzi and Vamvatsikos (2015)	$S_{\mathrm{a,gm}}(T_j) = \left[\prod_{j=1}^{5} S_{\mathrm{a}}(T_{\mathrm{S},j})\right]^{1/5}$	$T_{\mathrm{S},j}$ is the j^{th} selected period, and $T_{\mathrm{S},1}$~$T_{\mathrm{S},5}$ are T_2, min[$(T_1+T_2)/2$, $1.5T_2$], T_1, $1.5T_1$ and $2T_1$, respectively.
Zhang et al. (2018)	$S_v^* = [S_v(T_1)]^{0.5}[S_v(T_2)]^{0.5}$	
Housner (1952)	$HI = \int_{0.1}^{2.5} S_{\mathrm{v,p}}(T)dT$	$S_{\mathrm{v,p}}(T)$ is pseudo-spectral velocity at period T.
Thun et al. (1988)	$VSI = \int_{0.1}^{2.5} S_{\mathrm{v}}(T)dT$	
Bojórquez et al. (2017)	$IB_{\mathrm{sa}} = S_{\mathrm{a}}(T_1)^{0.4} S_{\mathrm{a}}(T_2)^{0.2} \left[\prod_{i=1}^{N} S_{\mathrm{a}}(T_{\mathrm{I},j})\right]^{2/(5N)}$	$T_{\mathrm{I},j}$ is the j^{th} period during T_1 and $2T_1$ with the same interval, i.e. 0.01; N is the number of spectral accelerations.
Eads et al. (2015)	$Sa_{\mathrm{avg}} = \left[\prod_{i=1}^{N} S_{\mathrm{a}}(T_{\mathrm{K},j})\right]^{1/N}$	$T_{\mathrm{K},j}$ is the j^{th} period during $0.2T_1$ and $3T_1$ with the same interval, i.e. 0.01; N is the number of spectral accelerations.
Other	$S_{\mathrm{v}}(T_1)$	

related to the spectral velocity are selected with the consideration of the fact that $\bar{S}_{\mathrm{v}}^{*}$ essentially consists of spectral velocities of multiple modes. In these IMs, I_{Np}, S_{avg}, S^{*} and S_{N1} consider the elongation of T_1. S_{12}, S_{N2}, IM_{12}, S_{123} and IM_{123} have similar expressions, but different exponents and the numbers of modes. In these IMs, S^{*}, S_{N1} and $S_{\mathrm{a,gm}}$ can account for the elongation of T_1. S_{12}, S_{N2}, IM_{12}, S_{123} and IM_{123} have similar mathematical expressions, but with different exponents and the different numbers of modes involved. Both IB_{sa} and S_{avg} can reflect the shape of the acceleration response spectrum in terms of its geometric means. The spectral accelerations at the first two vibration periods are included in IB_{sa} which has a narrower period range. For $\bar{S}_{\mathrm{v}}^{*}$, according to Eq. (15), for S1~S7, the optimal numbers of modes included in S1~S7 turn out to be 1, 2, 2, 2, 3, 3, 4 accordingly for the group of the near-field ground motions, and 2, 2, 2, 3, 3, 4, 4 for the far-field ground motions, accordingly.

Fig. 10 shows the correlation coefficients between the IMs and elastic IDR_{max} obtained by FSM-MSs corresponding to S1~S7. For the sake of discussion, the means (denoted by the dashed blue line) and coefficients of variation (COVs) (see the numbers in parentheses) of the correlation coefficients are used. The correlation coefficients of $\bar{S}_{\mathrm{v}}^{*}$ are found to have the highest mean of 0.96 and the lowest COV of 0.01 among 20 IMs, in either ground motion group, indicating a desirably stable and effective correlation with the elastic maximum ISD ratios, IDR_{max}. Another spectral velocity-based S_{v}^{*} has a similar efficiency to $\bar{S}_{\mathrm{v}}^{*}$ in the case of the far-field ground motions. However, for the near-field ground motions, its efficiency is obviously affected, exhibiting a decrease in the mean from 0.95 to 0.90 and an increase in the COV from 0.03 to 0.07. Compared with $\bar{S}_{\mathrm{v}}^{*}$, the relatively inferior performance of S_{v}^{*} can be roughly attributed to the identical combination coefficients used for different modes. For $S_{\mathrm{v}}(T_1)$, the means of the correlation coefficients are close to those of $\bar{S}_{\mathrm{v}}^{*}$, and the COVs exhibit a slight fluctuation in different groups of ground motions. As a result of not considering the high-mode effect, for S7 with the smaller value of δ_{ρ}, $S_{\mathrm{v}}(T_1)$ only has a correlation coefficient of 0.86 in the near-field ground motions. Although $\bar{S}_{\mathrm{a}}^{*}$ indicates the close mean (0.93) and COV (0.04) of the correlation coefficients to those of $\bar{S}_{\mathrm{v}}^{*}$ in the case of the near-field ground motions, its efficiency and stability are reduced when the far-field ground motions are considered. The efficiency and stability of IM_{123} and $\bar{S}_{\mathrm{a}}$ are basically acceptable, showing slightly lower means and slightly higher COVs compared with those of the proposed IM $\bar{S}_{\mathrm{v}}^{*}$. The performance of the rest of IMs is comparatively inferior to the above-mentioned IMs, from the aspect of the mean and COV of the correlation coefficients. PGA has the poorest performance among 20 IMs. PGV performs very well in the case of the near-field ground motion but not desirably in the far-field ground motions. Those spectral acceleration-based IMs with large weighting coefficients of $S_a(T_1)$, e.g. S_{12}, S_{123} and S_{N2}, are observed to fail to display a stable correlation with the elastic IDR_{max}. This can be explained by the increase in the fundamental period and mass-stiffness non-uniformities, especially in the case of the near-field ground motions. Those IMs considering period elongation effect or spectral shape, e.g., S^*, IB_{sa}, S_{N1}, $S_{a,gm}$ and S_{avg}, do not possess higher efficiency than those considering multiple vibration modes. It can be believed from the discussion above that, from the statistical aspect, the proposed IM $\bar{S}_v^*$ has the highest and most stable correlation with the elastic IDR_{max} among the 20 IMs.

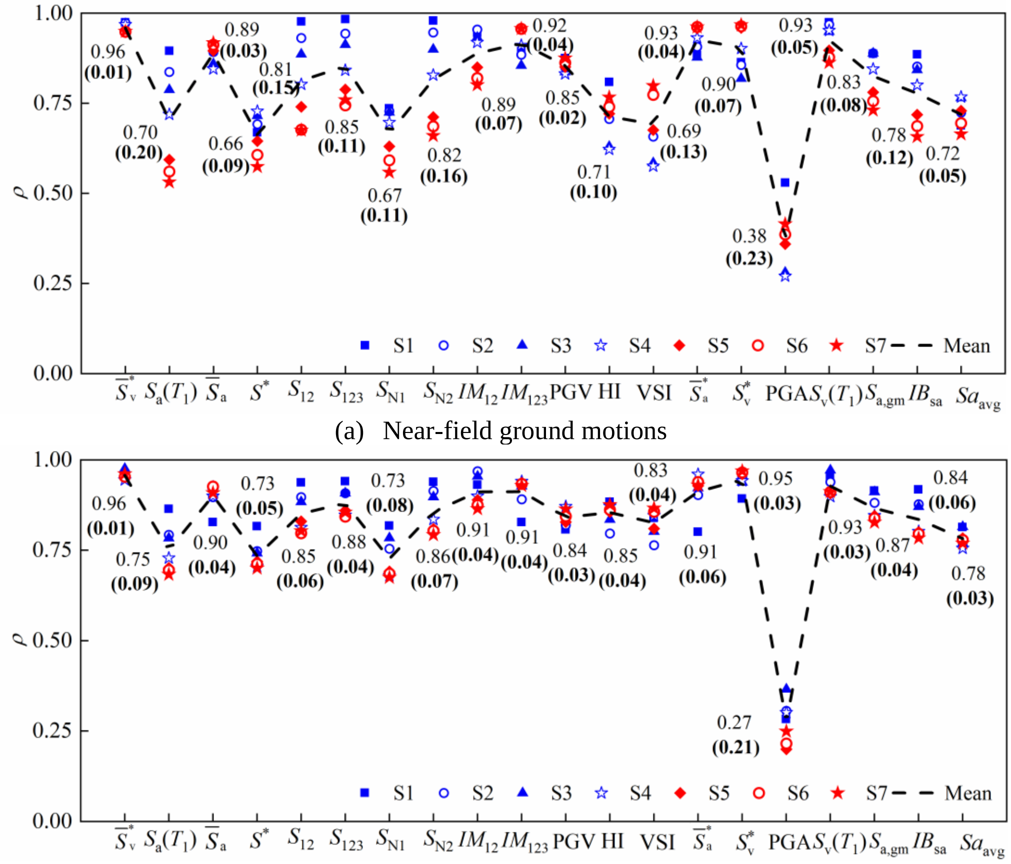

(a) Near-field ground motions

(b) Far-field ground motions

Fig. 10. Correlation coefficients between 20 IMs and elastic IDR_{max} of S1~S7

4.3. Further comparison of shortlisted intensity measures

4.3.1 Efficiency

As obvious differences in the structural height and the non-uniformities of mass and stiffness between S3 and S5 can be observed, a further comparison of the shortlisted IMs is performed based on their finite element models. For the sake of discussion, only those having the means of the correlation coefficients of all the ground motions (for both the near-field and far-field) not less than 0.90, i.e., $S_v(T_1)$, IM_{123}, $\overline{S}_a$, $\overline{S}_a^*$, S_v^* and $\overline{S}_v^*$, are selected to further evaluate their performance on the two super high-rise buildings, i.e., S3 and S5 which have obvious differences in the height and mass-stiffness non-uniformities, via the inelastic THAs with the ground motions. Fig. 11 shows the envelope curves of the inter-story drift ratios of S3 and S5 along the height under records from Tables 1 and 2. In consideration of the close relationship between the efficiency of the IM and the degree of structural damage, the following six seismic performance levels proposed by Li et al. (2021) for the frame-core tube structure are adopted to reveal the degree of structural damage of S3 and S5 under the selected records: full occupancy (FO), basic occupancy (BO), immediate occupancy (IO), delayed occupancy (DO), life safety (LS) and collapse prevention (CP). And the corresponding IDR_{max} at the boundaries are 1/755, 1/515, 1/215, 1/130 and 1/95. A higher seismic performance level indicates severe structural damage. Figs. 12 and 13 show in more detail about the relation between the six preliminarily selected IMs and the values of IDR_{max} of S3 and S5 under the near-field and far-field ground motions, respectively, along with the six performance levels. With the classified six performance levels, the distributions of IDR_{max} in different damage states using different IMs under the two groups of the ground motions can be clearly observed, as well as the slopes and correlation coefficients mentioned above. In the group of the near-field ground motions (see Fig. 12), 15 ground motions cause S3 to experience damages at the LS and CP levels while S5 experiences damages at the DO and IO levels excited with most of the near-field ground motions. S3 exhibits a larger possibility of experiencing more severe damage in the case of near-field ground motions. For the far-field ground motions, none of them can cause S3 and S5 to experience severe damage (e.g. LS or CP level). Figs. 12 and 13 also indicate that, for the ground motions in either near-field group or far-field group, the response data points of S3 tend to be located more closely around the regressive lines, resulting in the higher coefficients of S3 than those of S5. This may arise from more strengthened floors and more prominent mass-stiffness non-uniformities in S5. Its comparatively complex seismic response cannot be predicted with a desirable accuracy by a single IM.

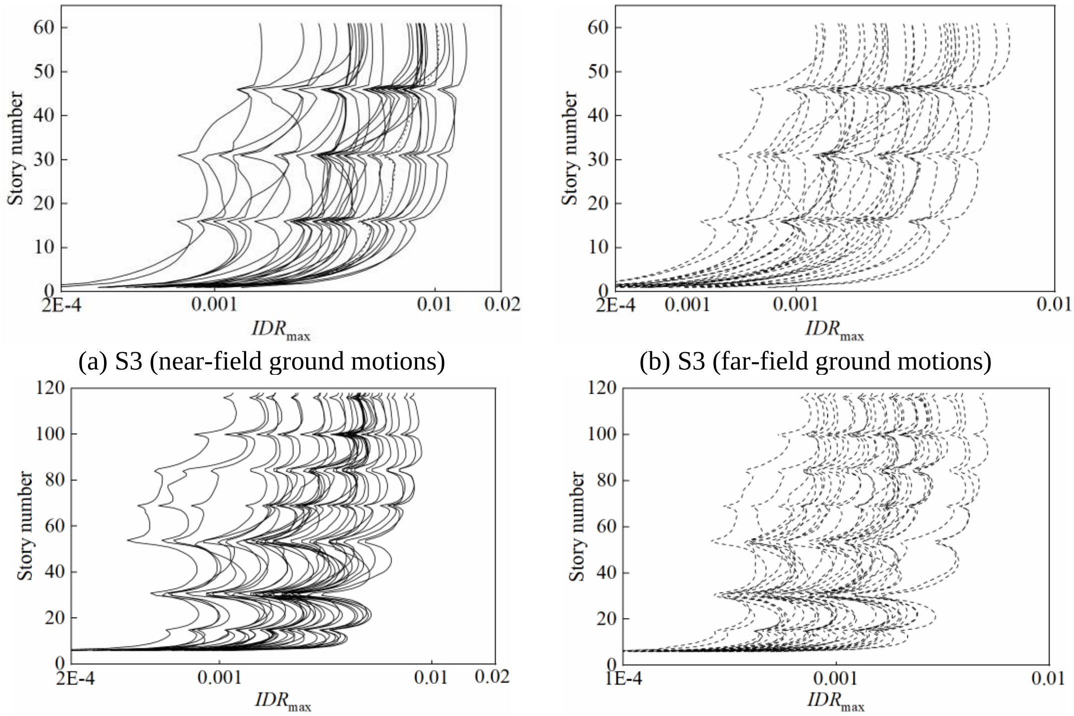

(a) S3 (near-field ground motions) (b) S3 (far-field ground motions)

(c) S5 (near-field ground motions) (d) S5 (far-field ground motions)

Fig. 11. Envelope curves of inter-story drift ratios of finite element

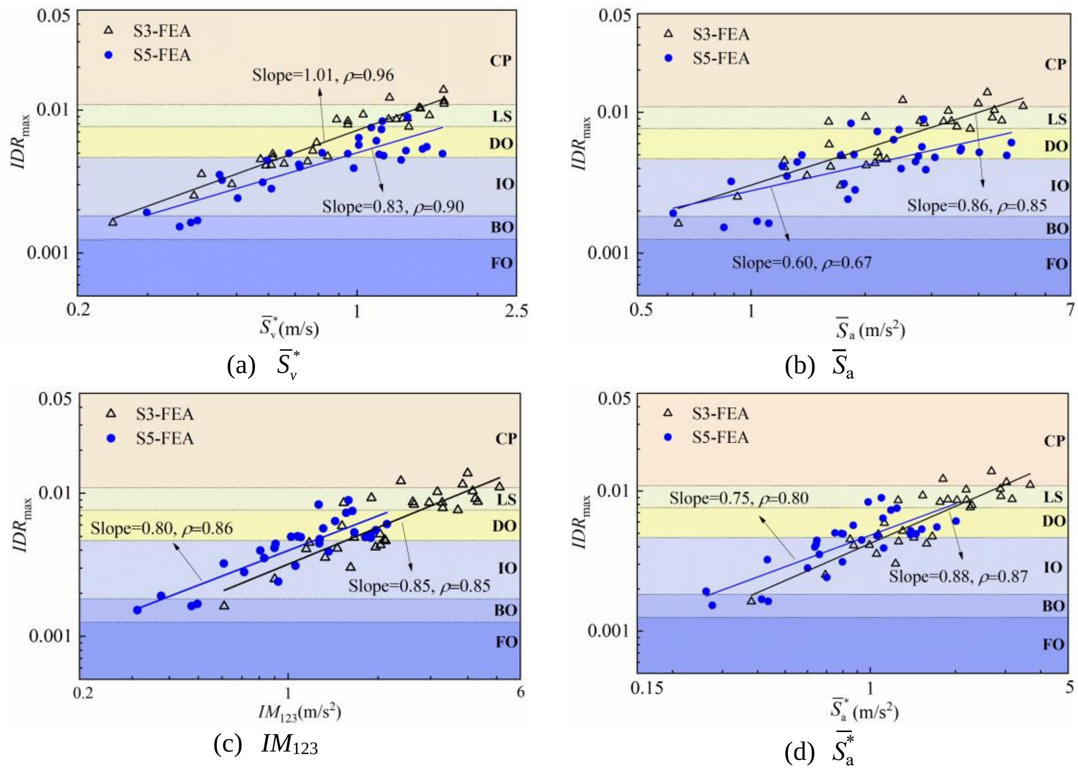

(a) $\overline{S}_v^*$ (b) $\overline{S}_a$

(c) IM_{123} (d) $\overline{S}_a^*$

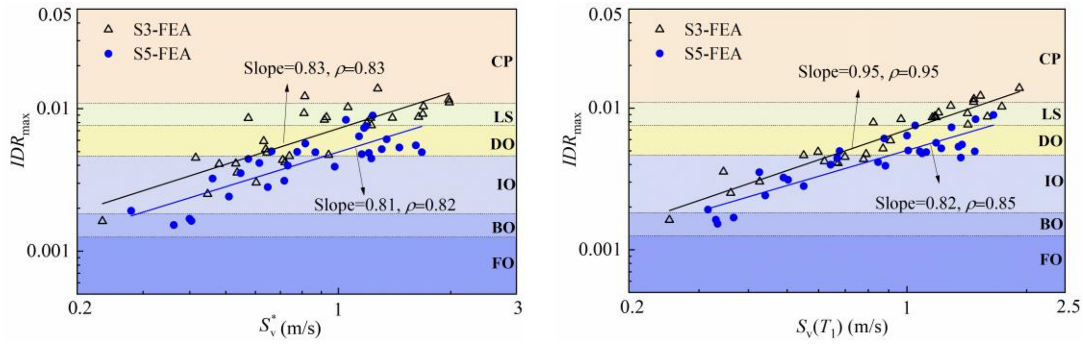

(e) S_v^* (f) $S_v(T_1)$

Fig. 12. Log-linear regressions of maximum ISD ratios and six IMs of S3 and S5 (Near-field ground motions)

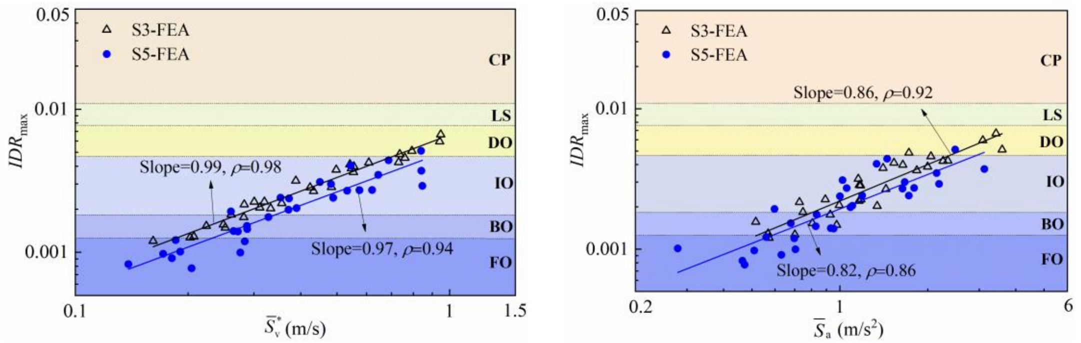

(a) $\bar{S}_v^*$ (b) $\bar{S}_a$

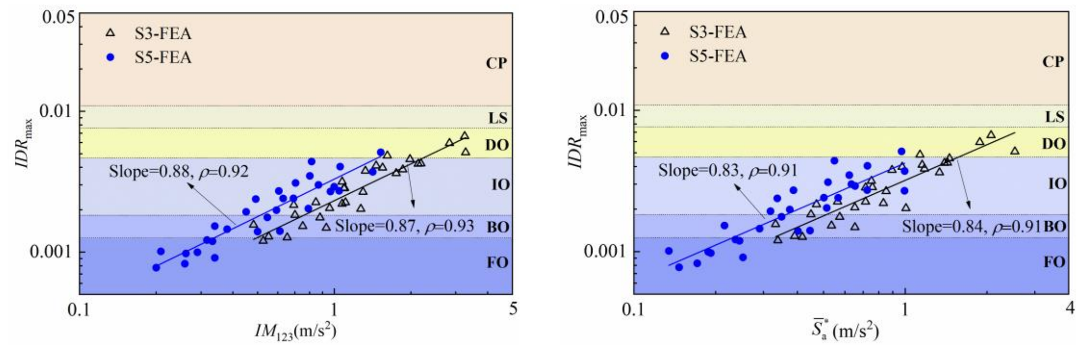

(c) IM_{123} (d) $\bar{S}_a^*$

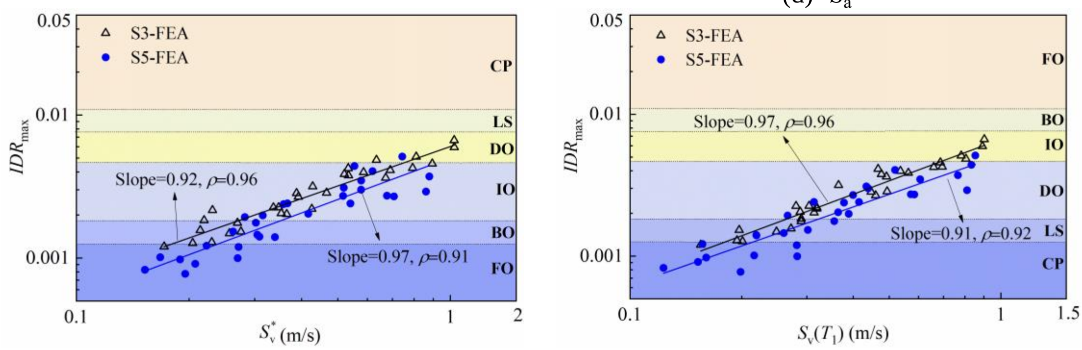

(e) S_v^* (f) $S_v(T_1)$

Fig. 13. Log-linear regressions of maximum ISD ratios and six IMs of S3 and S5 (Far-field ground motions)

To reach an overall evaluation of the performance of the six preliminarily selected IMs, in addition to the correlation coefficients of S3 and S5 determined based on the inelastic THAs (see the solid red circles and solid blue diamonds), the correlation coefficients of S1~S7 shown in Fig. 10 are also included in Fig. 14. Even for the case of the inelastic IDR_{max} of S3 and S5, $\bar{S}_{\mathrm{v}}^{*}$ still exhibits the highest correlation, with all the correlation coefficients not less than 0.90, among the six IMs for either group of the ground motions, although the differences are not so significant for some IMs. The correlation coefficients of S_{v}^{*} and $S_{\mathrm{v}}(T_1)$ based on the inelastic IDR_{max} of S3 and S5 are close to those of $\bar{S}_{\mathrm{v}}^{*}$ under the far-field ground motions. However, in the case of the near-field ground motions, the coefficients of S5 are reduced up to 0.82 and 0.85, respectively. The optimal numbers of modes included in $\bar{S}_{\mathrm{v}}^{*}$ and S_{v}^{*} are the same. The higher correlation of $\bar{S}_{\mathrm{v}}^{*}$ explains the rationality of the combination coefficients adopted. The spectral acceleration-based IM_{123} and $\bar{S}_{\mathrm{a}}^{*}$ can have correlation coefficients above 0.90 in the far-field ground motion case, but the coefficients become 0.85 and 0.86 in the group of the near-field ground motions. The correlation coefficients of $\bar{S}_{\mathrm{a}}$ and $\bar{S}_{\mathrm{a}}^{*}$ of S5 are below 0.80.

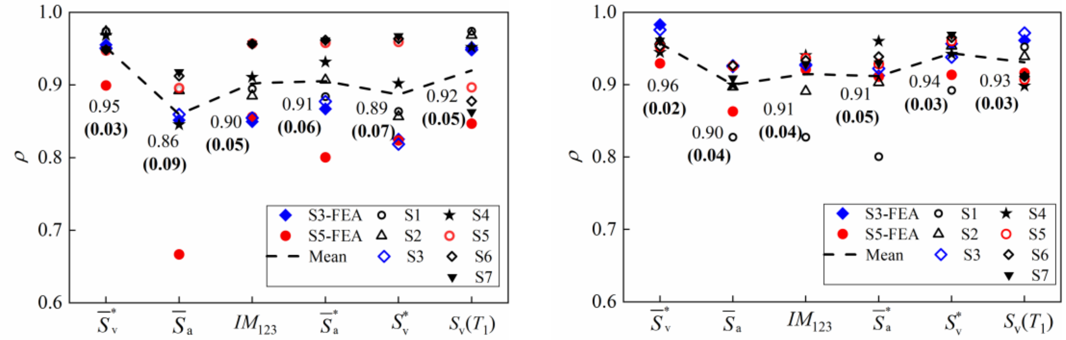

(a) Near-field ground motions (b) Near-field ground motions

Fig. 14. Correlation coefficients between preliminarily selected six IMs and IDR_{max} of S1~S7

With the correlation coefficients of S1~S7 shown in Fig. 10 added, the means of the correlation coefficients of $\bar{S}_{\mathrm{v}}^{*}$ under the near-field and far-field ground motions are 0.95 and 0.96, respectively, which are also higher than those of others. Although the means and coefficients of variation (COVs) of S_{v}^{*} and $S_{\mathrm{v}}(T_1)$ under the far-field ground motions are close to those of $\bar{S}_{\mathrm{v}}^{*}$, the COVs of the two IMs increase to 0.07 and 0.05 and the corresponding means become 0.89 and 0.92 under the near-field ground motions, respectively. Whether from the aspect of the mean or the COV of the correlation coefficients, $\bar{S}_{\mathrm{v}}^{*}$ exhibited desirably stable and efficient performance in either group of the ground motions. The means and COVs of the correlation coefficients of $\bar{S}_{\mathrm{a}}^{*}$ in the two groups of the ground motions are basically unchanged. However, in some cases, its correlation coefficients approach 0.80. The COV of the correlation coefficients of $\bar{S}_{\mathrm{a}}$ increases considerably from 0.04 to 0.09 as the far-field ground motion group is switched to the near-field ground motion group. Moreover, the mean of the correlation coefficients of $\overline{S}_{\mathrm{a}}$ is also the lowest among the six IMs in either ground motion group. It can be concluded, with some confidence, from the observations in Figs. 10 and 14 that, for either group of the ground motions, $\overline{S}_{\mathrm{v}}^{*}$ has exhibited a desirable level of stability and efficiency with $IDR_{\max}$ of structures having a broad range of periods and heights.

To verify the accuracy of the estimated optimal number of modes n_{opt} in Eq. (15), Fig. 15 provides the correlation coefficients between the $\overline{S}_{\mathrm{v}}^{*}$ with different numbers of modes and $IDR_{\max}$ of S3 and S5 obtained by finite element models. Based on Eq. (15), the n_{opt} of S3 is equal to 2 under both kinds of ground motions, while the n_{opt} of S5 is equal to 3 under both kinds of ground motions. It can be seen that the optimal number of modes obtained by the finite element model is the same as the estimated n_{opt}, which indicates that the accuracy of Eq. (15) is acceptable.

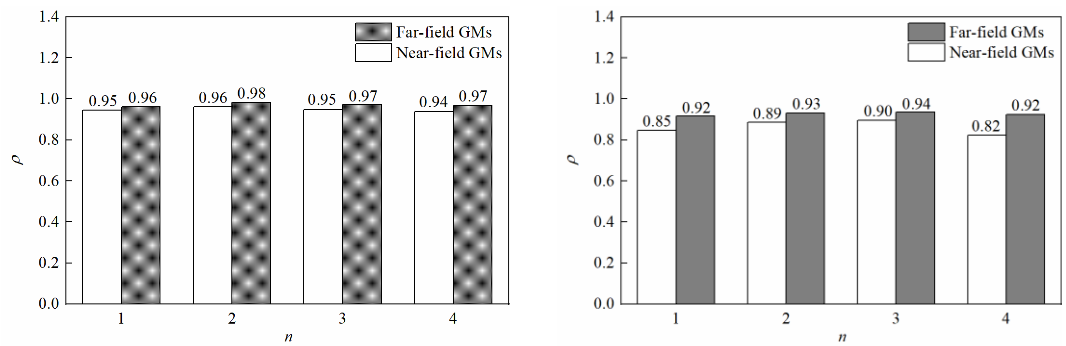

Fig. 15. Correlation coefficients between proposed IM with different number of modes and $IDR_{\max}$ calculated by finite element models

4.3.2 Sufficiency

A sufficient IM is defined as one that renders DMs conditionally independent of other characteristics of ground motions (Luco and Cornell 2007). As the deviations introduced by the magnitude M and the source-to-site distance R to the DM have been widely concerned (Dávalos and Miranda 2019), the sufficiency of the shortlisted IMs regarding M and R is studied here. In fact, it is quite challenging to prove the sufficiency of an IM in a an absolute manner (Ebrahimian and Jalayer 2021). A commonly-used approach to evaluate the sufficiency is to calculate the p-value obtained by the standard linear regression of the residual term ln($\varepsilon|IM$) in Eq. (2), i.e., the difference between the calculated and predicted DM, as a function of the ground motion parameters of interest (Khosravikia and Clayton 2020). With a certain significance level (usually 5%), the p-value is applied primarily to judge whether the null hypothesis (i.e., the slope of the linear regression between ln($\varepsilon|IM$) and the ground motion parameters of concern) can be rejected or not. If the p-value is less than 0.05, the null hypothesis is rejected. That is, an IM of concern is not sufficient. For other cases, the null hypothesis cannot be rejected. However, it is still unable to prove that an IM of concern is sufficient. For this purpose, previous studies put forward some evaluation indexes based on the variation in the probability density functions of a DM of concern before and after adding other ground motion parameters (Dhulipala et al. 2018; Yan et al. 2022). However, the threshold values used to judge whether an IM of concern is sufficient or not are still controversial. It is comparatively more practical and appropriate to select the most sufficient IM among the candidate Ims, by directly comparing their relative sufficiency. Thus, in addition to the p-value of the proposed IM, the relative sufficiency measure (RSM) proposed by Jalayer et al. (2012), which is based on the theory of relative entropy and has been used in some studies (Du et al. 2019; Minas and Galasso 2019), is calculated for other five Ims with respect to the proposed IM. By replacing the expectation with an average over a suite of ground motions, Ebrahimian et al. (2015) proposed the following approximate RSM of the intensity measure IM_2 relative to IM_1:

$$I(DM \mid IM_2 \mid IM_1) \approx \frac{1}{m}\sum_{j=1}^{m}\log_2 \frac{\beta_{DM|IM_1}\Phi\left[\dfrac{\ln DM_j - \ln(aIM_{2j}^{b})}{\beta_{DM|IM_2}}\right])}{\beta_{DM|IM_2}\Phi\left[\dfrac{\ln DM_j - \ln(aIM_{1j}^{b})}{\beta_{DM|IM_1}}\right]} \quad (16)$$

where, Φ(.) is the standard Gaussian probability density function; a and b are regressed coefficients in Eq. (2); $\beta_{DM|IM_1}$ is the standard derivation obtained by the log-linear regression between DM and IM_1; if the RSM is positive, it means that on average, IM_2 provides more more sufficient than IM_1 for predicting the DM, and if the RSM is zero, it indicates that the two Ims are equally sufficient.

Figs. 16 and 17 present the linear regression of ln($\varepsilon|IM$) on ln® and M, respectively. It can be seen that all the p-values are greater than 0.05, indicating that the null hypothesis of the sufficiency of the proposed IM cannot be rejected. Fig. 18 further presents the RSMs of the other five Ims with respect to the proposed IM. Among the six Ims, the proposed IM is observed to be most sufficient for predicting the response of S3 and S5.

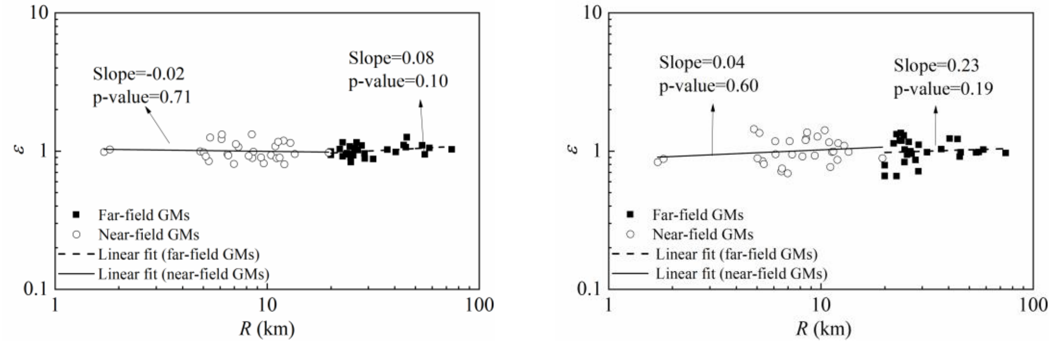

(a) S3 (b) S5

Fig. 16. Linear regression of the ln(ε|IM) on ln(R) by proposed IM

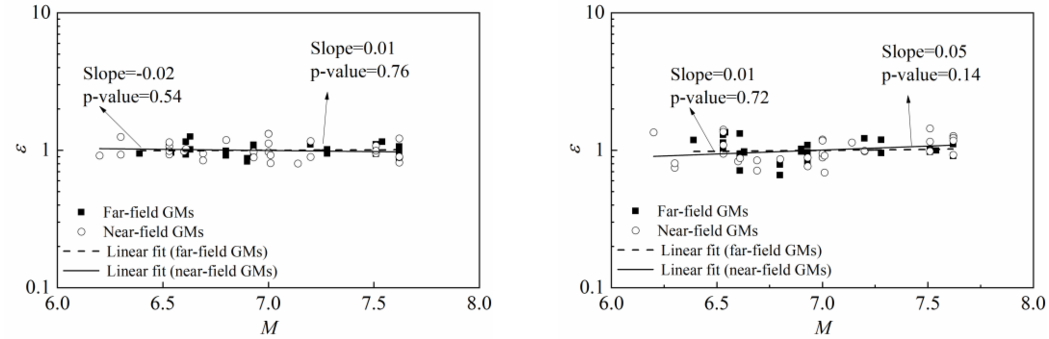

(a) S3 (b) S5

Fig. 17. Linear regression of the ln(ε|IM) on M by proposed IM

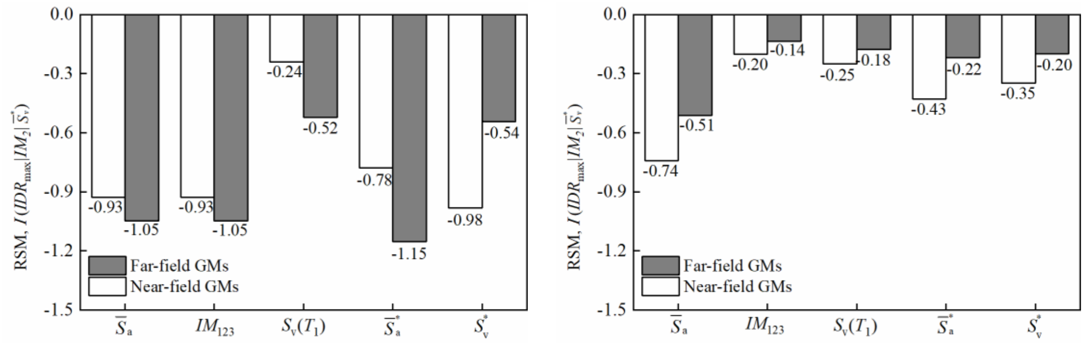

(a) S3 (b) S5

Fig. 18. Relative sufficiency measure of other shortlisted IMs with respect to proposed IM

4.3.3 Scaling robustness

The scaling robustness can be interpreted as a feature of generating unbiased structural responses toward the scaling of ground motion records (Tothong and Luco 2007). Similar to sufficiency, scaling robustness can be evaluated in terms of the slope and p-values obtained by the standard logarithmic linear regression of the $IDR_{\max}$ with respect to the scaling factor. The scaling robustness of an IM can be declared when the estimated slope is close to zero. A p-value lower than 0.05 indicates that the slope is significantly different from zero, which means the IM is not robust with respect to scaling. To make more analysis into the severe nonlinear stage, each record is scaled according to the maximum $\overline{S}_{\mathrm{v}}^{*}$ of the 60 ground motion records in Tables 1 and 2, which is 3.288 m/s. The corresponding record is the first near-field record in Table 1, and its PGA is 0.874 g.

Due to the heavy computational burden associated with the nonlinear time-history analysis of super high-rise buildings, only S5 is adopted to evaluate the scaling robustness of $\bar{S}_{\mathrm{v}}^{*}$. To reveal the levels of structural damage under scaled records, the number of scaled records corresponding to each seismic performance level of S5 is presented in Fig. 19. Compared with Figs. 12 and 13, the numbers of records corresponding to the severe damage level increase obviously under the scaled records, which means the purpose of the scaling is achieved. The logarithmic linear regression between the scaling factor and corresponding $IDR_{\max}$ is shown in Fig. 20. It can be seen that the scaling factor is relatively evenly distributed between 1 and 10, indicating the obvious difference between the $\bar{S}_{\mathrm{v}}^{*}$ of the selected ground motions and further proving the diversity of these ground motions. The slope of the logarithmic regression is less than 0.1 and the p-value is greater than 0.05, implying the scaling robustness of $\bar{S}_{\mathrm{v}}^{*}$.

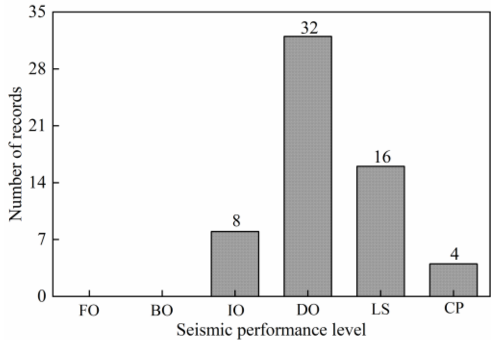

Fig. 19. Number of scaled ground motions corresponding to different seismic performance levels of S5

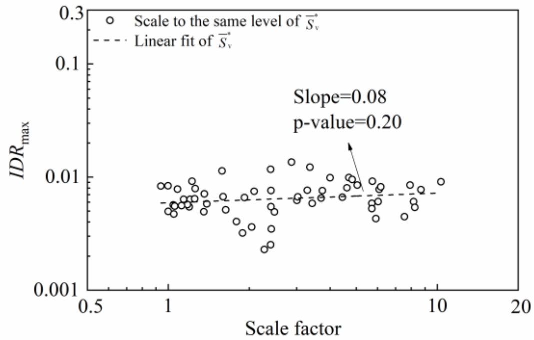

Fig. 20. Log-linear regression between the scaling factor and corresponding $IDR_{\max}$ of S5

5. Conclusion

1) The physical background of spectral velocity used as the core element of the proposed IM $\bar{S}_{\mathrm{v}}^{*}$ with a specific concern of super high-rise buildings has been systematically justified. In addition to its potentially close link with equivalent velocity and damage-related hysteretic energy dissipation, the spectral velocities at the first several periods, especially that at the fundamental period, are observed, via the case study of S3 and S5, to exhibit more desirable correlation with the maximum inter-story drift (ISD) ratios than corresponding spectral accelerations. The exponential function-based combination pattern of $\bar{S}_{\mathrm{v}}^{*}$ can independently reflect the influence of each spectral velocity on the structural demand measure (DM) in logarithmic form.

2) The combination coefficients and optimal number of modes involved in $\bar{S}_{\mathrm{v}}^{*}$ are adaptive and case-

independent. These parameters can be quickly determined by the fundament period T_1, the second-to-fundamental period ratio T_2/T_1 and non-uniform coefficient of linear density δ_ρ, which all can be estimated even during the preliminary design stage of buildings without detailed structural design information. The determination of the optimal number of modes can reflect the higher contribution proportion of the lower modes to the maximum ISD ratios of super high-rise buildings under the near-field ground motions, compared with the far-field ground motions. When all the combination coefficients are equally taken as 0.5 and the optimal number of modes is taken as 2, $\bar{S}_{\mathrm{v}}^{*}$ can be converted into its precedent version S_{v}^{*}.

3) The two-stage performance evaluation strategy developed herein can reduce the case dependency to the largest extent of the justification of efficiency. With the use of the flexure-shear coupled models (FSM-MS) in the first stage, the elastic ISD ratios of structural finite element models and virtual FSM-MSs that cover the most range of building heights and vibration periods can be efficiently obtained. Some preliminarily unqualified IMs can be excluded in this stage. The inelastic time history analyses performed in the second stage on two super high-rise buildings can reach a more comprehensive evaluation for those preliminarily qualified IMs. By using the two-stage performance evaluation strategy, the stability of IMs involved can be identified as well as the efficiency.

4) The case study using the two-stage performance evaluation strategy indicates that the proposed IM $\bar{S}_{\mathrm{v}}^{*}$ has exhibited the superior stability and efficiency among 20 IMs, for either group of the ground motions. Compared with S_{v}^{*}, $\bar{S}_{\mathrm{v}}^{*}$ is more capable of describing the contribution of the spectral velocity at the second period to the efficiency. The spectral acceleration-based IMs with power functions, i.e., $S_{\mathrm{a}}(T_1)$-based S_{12}, S_{123}, S_{N2}, and those addressing the period elongation effect or spectral shape, i.e., S^*, IB_{sa}, S_{N1}, $S_{\mathrm{a,gm}}$ and S_{avg}, fail to display high efficiency in the correlation with maximum ISD ratios. They are believed to be inappropriate for super high-rise buildings. The sufficiency and scaling robustness of $\bar{S}_{\mathrm{v}}^{*}$ is also observed to be desirable among the six shortlisted IMs.

5) Although the case study shows that the proposed IM $\bar{S}_{\mathrm{v}}^{*}$ is highly correlated with the maximum ISD ratios of super high-rise buildings, its correlation with other structural demand measures (DMs), e.g., the maximum floor acceleration, is unknown. In addition, the correlation of $\bar{S}_{\mathrm{v}}^{*}$ with the severe damage or even collapse response that super high-rise building structures may experience under strong ground motions also needs to be further investigated.

Acknowledgements

The authors would like express their gratitude to the financial support from the National Natural Science Foundation of China (Grant No. 52078105) and the Fundamental Research Funds for the Central Universities (Grant No. DUT19GJ208).

References

[1] Akiyama, H. 1985. *Earthquake-resistant Limit-state Design for Buildings.* University of Tokyo Press, Tokyo, Japan.

[2] Alonso-Rodríguez, A. and Miranda, E. 2016. "Dynamic behavior of buildings with non-uniform stiffness along their height assessed through coupled flexural and shear beams." *Bulletin of Earthquake Engineering*, 14(12), 3463-3483.

[3] Ancheta, T. D., Darragh, R. B., Stewart, J. P., Seyhan, E., Silva, W. J., Chiou, B. S., Wooddell, K. E., Graves, R. W., Kottke, A. R., Boore, D. M., Kishida, T., and Donahue, J. L. 2014. "NGA-West2 database." *Earthquake Spectra*, 30(3), 989-1005.

[4] Avşar, Ö., and Özdemir, G. 2013. "Response of seismic-isolated bridges in relation to intensity measures of ordinary and pulselike ground motions." *Journal of Bridge Engineering*, 18(3), 250-260.

[5] Baker, J. W. 2007. "Quantitative classification of near-fault ground motions using wavelet analysis." *Bulletin of the Seismological Society of America*, 97(5), 1486-1501.

[6] Bojórquez, E., and Iervolino, I. 2011. "Spectral shape proxies and nonlinear structural response." *Soil Dynamics and Earthquake Engineering*, 31(7), 996-1008.

[7] Bojórquez, E., Chávez, R., Reyes-Salazar, A., Ruiz, S. E., and Bojórquez J. 2017. "A new ground motion intensity measure I_B." *Soil Dynamics and Earthquake Engineering*, 99, 97-107.

[8] Chopra, A. K. 2016. *Dynamics of structures: Theory and applications to earthquake engineering.* University of California at Berkeley (5th edition), Pearson Education Inc., Boston, U.S.A.

[9] Cordova, P. P., Deierlein, G. G., Mehanny, S. S. F., and Cornell, C. A. 2001. "Development of a two-parameter seismic intensity measure and probabilistic assessment procedure." *Proceedings of the 2nd U.S.-Japan Workshop on Performance-based Earthquake Engineering Methodology for Reinforced Concrete Building Structures*, Sapporo, Hokkaido, Japan, September 11-13.

[10] Dávalos, E. and Miranda, E. 2019. “Filtered incremental velocity: a novel approach in intensity measures for seismic collapse estimation.” *Earthquake Engineering and Structural Dynamics*, 48(12), 1384-1405.

[11] Du, A., Padgett, J. E., and Shafieezadeh, A. 2019. “A posteriori optimal intensity measures for probabilistic seismic demand modeling.” *Bulletin of Earthquake Engineering*, 17(2), 681-706.

[12] Dhulipala, S. L., Rodriguez-Marek, A., Ranganathan, S., and Flint, M. M. 2018. “A site-consistent method to quantify sufficiency of alternative IMs in relation to PSDA.” *Earthquake Engineering and Structural Dynamics,* 47(2), 377-396.

[13] Ebrahimian, H., and Jalayer, F. 2021. “Selection of seismic intensity measures for prescribed limit states using alternative nonlinear dynamic analysis methods.” *Earthquake Engineering and Structural Dynamics,* 50(5), 1235-1250.

[14] Ebrahimian, H., Jalayer, F., Lucchini, A., Mollaioli, F., and Manfredi, G. 2015. “Preliminary ranking of alternative scalar and vector intensity measures of ground shaking.” *Bulletin of Earthquake Engineering*, 13(10), 2805-2840.

[15] Eads, L., Miranda, E., and Lignos, D. G. 2015. “Average spectral acceleration as an intensity measure for collapse risk assessment.” *Earthquake Engineering and Structural Dynamics*, 44(12), 2057-2073.

[16] Fu, S., He, Z., Li, Z. 2015. “Shared memory parallel computing procedures for nonlinear dynamic analysis of super high-rise buildings.” *Proceedings of the 2nd International Conference on Performance-Based and Life-Cycle Structural Engineering*, Brisbane, Australia, December 9-11.

[17] Filippou, F. C., Popov, E. P., and Bertero, V. V. 1983. *Effects of bond deterioration on hysteretic behavior of reinforced concrete joints*. EERC Report 83-19, Earthquake Engineering Research Center, University of California, Berkeley, California, U.S.A.

[18] Housner, G. W. 1952. “Spectrum intensity of strong motion earthquakes.” *Proceedings of the Symposium on Earthquakes and Blast Effects on Structures*, Los Angeles, U.S.A., June 26-28.

[19] Housner, G. W. 1956. “Limit design of structures to resist earthquakes.” *Proceedings of 1st World Conference on Earthquake Engineering,* Berkeley, California, U.S.A., May 1-13.

[20] He, X., and Lu, Z. 2019. “Seismic fragility assessment of a super tall building with hybrid control strategy using IDA method.” *Soil Dynamics and Earthquake Engineering*, 123, 278-291.

[21] He, Z., and Sun, C. 2018. “Seismic response analysis of super high-rise frame-core structures using

improved nonlinear layered shell model.” *Engineering Mechanics*, 35(6), 173-181. [in Chinese].

[22] Jalayer, F., Beck, J. L., and Zareian, F. 2012. “Analyzing the sufficiency of alternative scalar and vector intensity measures of ground shaking based on information theory.” *Journal of Engineering Mechanics*, 138(3), 307-316.

[23] Khosravikia, F., and Clayton, P. 2020. “Updated evaluation metrics for optimal intensity measure selection in probabilistic seismic demand models.” *Engineering Structures*, 202, 109899.

[24] Kazantzi, A. K., and Vamvatsikos, D. 2015. “Intensity measure selection for vulnerability studies of building classes.” *Earthquake Engineering and Structural Dynamics*, 44(15), 2677-2694.

[25] Kohrangi, M., Vamvatsikos, D., and Bazzurro, P. 2019. “Pulse-like versus non-pulse-like ground motion records: spectral shape comparisons and record selection strategies.” *Earthquake Engineering and Structural Dynamics*, 48(1), 46-64.

[26] Luco, N., and Cornell, C. A. 2007. “Structure-specific scalar intensity measures for near-source and ordinary earthquake ground motion.” *Earthquake Spectra*, 23(2), 357-392.

[27] Lai, X., He, Z., and Wu, Y. 2021. “Elastic inter-story drift seismic demand estimate of super high-rise buildings using coupled flexural-shear model with mass and stiffness non-uniformities.” *Engineering Structures*, 226, 111378.

[28] Lu, X., Lu, X., Guan, H., and Ye, L. 2013. “Comparison and selection of ground motion intensity measures for seismic design of super high-rise buildings.” *Advances in Structural Engineering*, 16(7), 1249-1262.

[29] Lin, L., Naumoski, N., Saatcioglu, M., and Foo, S. 2010. “Improved intensity measures for probabilistic seismic demand analysis. part 1: development of improved intensity measures.” *Canadian Journal of Civil Engineering*, 38(1), 79-88.

[30] Lu, X., Ye, L., Lu, X., Li, M., and Ma, X. 2013. “An improved ground motion intensity measure for super high-rise buildings.” *Science China Technological Sciences*, 56(6), 1525-1533.

[31] Li, Y., Yang, Q., Jiang, H., and Jin, G. 2021. “Study of performance-based inter-story drift angle limits for high-rise concrete-filled steel tube frame-steel reinforced concrete corewall structures.” Building Structure, 51(23), 69-75. [in Chinese].

[32] Li, S., and Xie, L. 2007. “Progress and trend on near-field problem in civil engineering.” *Acta Seismologica Sinica*, 20(1), 105-114.

[33] Mohd-Hisham, M. Y. “Nonlinear Analysis of Prestressed Concrete Structures under Monotonic and

Cycling Loads." Ph.D. dissertation, University of California, Berkeley, 1994.

[34] Ministry of Housing and Urban-Rural Development of the People's Republic of China. 2014. *Code for seismic design of buildings*. GB50011-2010. China Architecture and Building Press, Beijing, China.

[35] Ministry of Land, Infrastructure, Transport and Tourism. 2005. *Japanese building standard law.* JBSL. Ministry of Land, Infrastructure, Transport and Tourism, Tokyo, Japan.

[36] Minas, S., and Galasso, C. 2019. "Accounting for spectral shape in simplified fragility analysis of case-study reinforced concrete frames." *Soil Dynamics and Earthquake Engineering*, 119, 91-103.

[37] Miranda, E., and Taghavi, S. 2005. "Approximate floor acceleration demands in multistory buildings. I, Formulation." *Journal of Structural Engineering*, 131(2), 203-211.

[38] Montgomery, D. C., Peck, E. A., and Vining, G. G. 2021. *Introduction to linear regression analysis.* (6th edition). John Wiley & Sons,Inc., Hoboken, New Jersey, U.S.A.

[39] Prasanth, T., Ghosh, S. and Collins, K. R. 2008. "Estimation of hysteretic energy demand using concepts of modal pushover analysis." *Earthquake Engineering and Structural Dynamics*, 37, 975-990.

[40] Qiu, Y., Zhou, C., and A, S. 2020. "Correlation between earthquake intensity parameters and damage indices of high-rise RC chimneys." *Soil Dynamics and Earthquake Engineering*, 137, 106282.

[41] Shome, N., and Cornell, C. A. 1999. *Probabilistic seismic demand analysis of non-linear structures.* Report No. RMS-35. RMS Program, Stanford University, Stanford, California, U.S.A.

[42] Spacone, E., Filippou, F. C., and Taucer, F. 1996. "Fiber beam-column model for nonlinear analysis of R/C frames." *Earthquake Engineering and Structural Dynamics*, 25(7), 711-25.

[43] Su, N., Lu, X., Zhou, Y., and Yang, T. 2017 "Estimating the peak structural response of high-rise structures using spectral value-based intensity measures." *The Structural Design of Tall and Special Buildings*, 26(8), e1356.

[44] Tothong, P., and Luco, N. 2007. "Probabilistic seismic demand analysis using advanced ground motion intensity measures." *Earthquake Engineering and Structural Dynamics*, 36(13), 1837-1860.

[45] Thun. J. L. V., Rochim, L. H., Scott, G. A., and Wilson, J. A. 1988. "Earthquake ground motions for design and analysis of dams." *Proceedings of Earthquake Engineering and Soil Dynamics II-Recent Advances in Ground-Motion Evaluation*, Geotechnical Special Publication, Park City, Utah, U.S.A.,

June 27-30.

[46] Vamvatsikos, D., and Cornell, C. A. 2005. “Developing efficient scalar and vector intensity measures for IDA capacity estimation by incorporating elastic spectral shape information.” *Earthquake Engineering and Structural Dynamics*, 34(13), 1573-1600.

[47] Yan, Y., Xia, Y., Yang, J., and Sun, L. 2022. “Optimal selection of scalar and vector-valued seismic intensity measures based on Gaussian Process Regression.” *Soil Dynamics and Earthquake Engineering*, 152, 106961.

[48] Yakut, A., and Yılmaz, H. 2008. “Correlation of deformation demands with ground motion intensity.” *Journal of Structural Engineering*, 134(12), 1818-1828.

[49] Ye, L., Ma, Q., Miao, Z., Guan, H., and Zhuge, Y. 2013. “Numerical and comparative study of earthquake intensity indices in seismic analysis.” *The Structural Design of Tall and Special Buildings*, 22(4), 362-381.

[50] Zhang, Y., He, Z., and Yang, Y. 2018. “A spectral-velocity-based combination-type earthquake intensity measure for super high-rise buildings.” *Bulletin of Earthquake Engineering*, 16(2), 643-677.

[51] Zhang, Y., He, Z., Lv, W., and Yang, Y. 2018. “A spectral-acceleration-based linear combination-type earthquake intensity measure for high-rise buildings.” *Journal of Earthquake Engineering*, 22(8), 1479-1580.

[52] Lu, X., Su, N., and Zhou Y. 2015. “A benchmark model of mega-tall buildings and analysis of its seismic responses.” *Structural Engineer*, 31(4), 100-107. [in Chinese]